

Chromatin structure dynamics during the mitosis-to-G1 phase transition

<https://doi.org/10.1038/s41586-019-1778-y>

Received: 17 March 2019

Accepted: 2 October 2019

Published online: 27 November 2019

Haoyue Zhang¹, Daniel J. Emerson², Thomas G. Gilgenast², Katelyn R. Titus², Yemin Lan³, Peng Huang¹, Di Zhang^{1,3}, Hongxin Wang¹, Cheryl A. Keller⁴, Belinda Giardine⁴, Ross C. Hardison⁴, Jennifer E. Phillips-Cremens^{2*} & Gerd A. Blobel^{1,3*}

Features of higher-order chromatin organization—such as A/B compartments, topologically associating domains and chromatin loops—are temporarily disrupted during mitosis^{1,2}. Because these structures are thought to influence gene regulation, it is important to understand how they are re-established after mitosis. Here we examine the dynamics of chromosome reorganization by Hi-C after mitosis in highly purified, synchronous mouse erythroid cell populations. We observed rapid establishment of A/B compartments, followed by their gradual intensification and expansion. Contact domains form from the ‘bottom up’—smaller subTADs are formed initially, followed by convergence into multi-domain TAD structures. CTCF is partially retained on mitotic chromosomes and immediately resumes full binding in ana/telophase. By contrast, cohesin is completely evicted from mitotic chromosomes and regains focal binding at a slower rate. The formation of CTCF/cohesin co-anchored structural loops follows the kinetics of cohesin positioning. Stripe-shaped contact patterns—anchored by CTCF—grow in length, which is consistent with a loop-extrusion process after mitosis. Interactions between *cis*-regulatory elements can form rapidly, with rates exceeding those of CTCF/cohesin-anchored contacts. Notably, we identified a group of rapidly emerging transient contacts between *cis*-regulatory elements in ana/telophase that are dissolved upon G1 entry, co-incident with the establishment of inner boundaries or nearby interfering chromatin loops. We also describe the relationship between transcription reactivation and architectural features. Our findings indicate that distinct but mutually influential forces drive post-mitotic chromatin reconfiguration.

The global restructuring of chromosomal architecture during the progression from mitosis into G1 phase provides an opportunity to examine hierarchies and mechanisms of chromosome organization³ (Extended Data Fig. 1a). We performed *in situ* Hi-C experiments⁴ at defined time points after mitosis following nocodazole-induced prometaphase arrest–release in G1E-ER4 cells, a well-characterized subline⁵ of the mouse erythroblast line G1E (Fig. 1a). To ensure maximal purity of cell populations, we used a fluorescence-activated-cell-sorting (FACS)-based isolation strategy based on cell cycle markers and DNA content (Extended Data Fig. 1b, c; Supplementary Methods). *In situ* Hi-C collectively yielded around 2 billion uniquely mapped interactions, with high concordance between biological replicates (Extended Data Fig. 1d–f). Consistent with previous studies, compartments are largely eliminated in prometaphase^{1,2} (Fig. 1b). In ana/telophase—the earliest examined interval—compartments are already detectable visually and by eigenvector decomposition, and gain in intensity as cells advance into G1 (Fig. 1b–d; Extended Data Fig. 2a–c). This is consistent with the results of a multiplexed 4C-seq study, which reported the early establishment

of compartments after mitosis⁶. As expected, the A-type compartment is associated with active histone marks⁷ (Extended Data Fig. 2d). As cells proceed towards late G1, the characteristic checkerboard pattern of compartments visually expands away from the diagonal, leading to increased interaction frequencies at large (>100 Mb) distance scales (Fig. 1b, Extended Data Fig. 2e, f). Quantification of compartmentalization at different genomic distance scales across all cell cycle stages revealed a progressive gain of compartmentalization among distant (>100 Mb) genomic regions, confirming the expansion of compartments after mitosis (Extended Data Fig. 2g–i; Supplementary Methods). Therefore, a major reconfiguration of genome structure occurs during the prometaphase–G1 phase transition, involving a rapid establishment, progressive strengthening, and expansion of A/B compartments throughout the chromosome.

Next we examined the formation of topologically associating domains (TADs) and nested subTADs after mitosis using 3DNetMod⁸. We identified a total of 8,082 contact domains that are progressively gained from prometaphase to mid G1 (Fig. 2a; Supplementary Table 1).

¹Division of Hematology, The Children's Hospital of Philadelphia, Philadelphia, PA, USA. ²Department of Bioengineering, University of Pennsylvania, Philadelphia, PA, USA. ³Perelman School of Medicine, University of Pennsylvania, Philadelphia, PA, USA. ⁴Department of Biochemistry and Molecular Biology, Pennsylvania State University, University Park, PA, USA. *e-mail: jcremins@seas.upenn.edu; blobel@email.chop.edu

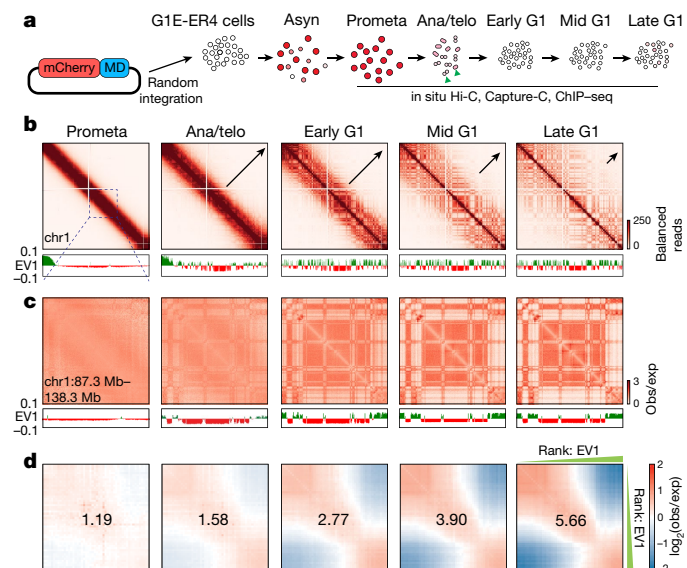


Fig. 1 | Early appearance and progressive strengthening and expansion of A/B compartments after mitosis. **a**, Schematic showing the reporter gene encoding mCherry fused to the mouse cyclin B mitotic degradation domain (mCherry–MD) and the expected mCherry signal at each cell cycle stage. Green arrowheads indicate sorting of cells in anaphase or telophase (ana/telo). Asyn, asynchronous; prometa, prometaphase. **b**, Hi-C contact maps showing the restoration of chromatin A/B compartments of chromosome 1 after mitosis, along with genome browser tracks showing eigenvector 1 values. Bin size, 250 kb. Arrows indicate expansion of compartments. **c**, A magnified view (chr1:87.3 Mb–138.3 Mb) of **b** revealing the clear plaid-like compartment pattern in ana/telophase. **d**, Saddle plots showing the genome-wide compartment strength over time.

Establishment of boundaries and enrichment of intradomain interactions were observed at newly emerging domains, thereby validating our domain-calling approach (Extended Data Fig. 3a–e). Previous studies have reported a complete loss of domains in prometaphase^{1,2}. However, despite considerable attenuation, residual domain- and boundary-like structures are still detectable visually and algorithmically in prometaphase cells (Extended Data Fig. 3f). To rule out contamination by G1 cells as a cause of prometaphase domain detection, we simulated *in silico* admixing with up to 20% of G1 chromosomes. Even a G1 contribution of 20%—which far exceeds the observed interphase cell contamination of up to 2%—did not reproduce patterns observed in prometaphase (Extended Data Fig. 3f–h); this suggests that prometaphase domain- and boundary-like features are not due to the presence of G1 phase cells. Residual domain boundaries in prometaphase are enriched with active histone marks and transcription start sites⁹ (Extended Data Fig. 3i, j).

Formation of nested domain structures may occur through the convergence of previously emerged subTADs (bottom-up), the partitioning of initially formed TADs into subTADs (top-down), or the simultaneous appearance of both contact domain types (Extended Data Fig. 4a). On average, contact domains that are established at time points later in G1 are larger than those called at earlier stages of the cell cycle (Fig. 2a, b); this observation favours the bottom-up formation scenario. To further test this model, we categorized all contact domains into 2,899 TADs and 5,183 subTADs on the basis of their hierarchical organization (Fig. 2c). Notably, higher proportions of subTADs are detected in prometaphase or ana/telophase compared to the TADs that encompass them, which suggests that subTADs tend to assemble more rapidly (Fig. 2c). Once established, the majority of TADs remain unchanged without further subdivisions, disfavoured the ‘top-down’ model (Extended Data Fig. 4b). By contrast, 85.4% and 69.1% of subTADs called in prometaphase and ana/telophase, respectively, converge into larger domains

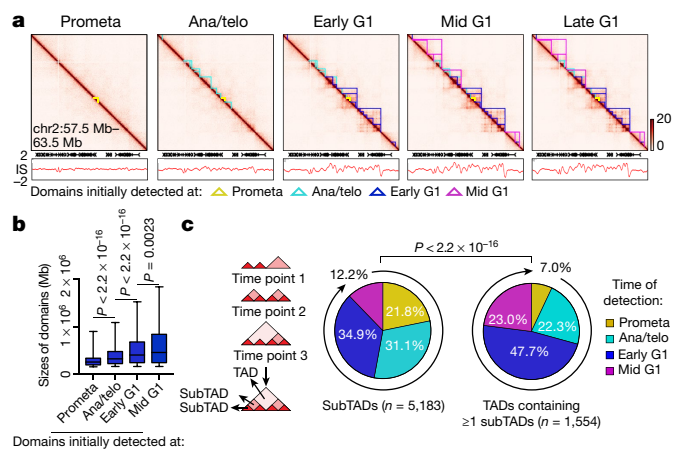


Fig. 2 | Contact domains develop from the bottom up after mitosis. **a**, Hi-C contact maps coupled with insulation score tracks (chr2: 57.5 Mb–63.5 Mb). Domains emerging at each stage of the cell cycle are demarcated by colour-coded lines. Bin size, 10 kb. Colour bar denotes *q*-normed reads. **b**, Sizes of domains newly detected at prometaphase ($n = 1,528$), ana/telophase ($n = 2,394$), early G1 ($n = 2,995$) and mid G1 ($n = 1,165$). For all box plots, centre lines denote medians; box limits denote 25th–75th percentile; whiskers denote 5th–95th percentile. *P* values were calculated by a two-sided Mann–Whitney *U*-test. **c**, Left, schematic showing the partition of domains into TADs or subTADs. TADs are domains that are not encompassed by any other domains; subTADs are domains that are completely encompassed by other domains. Right, pie charts of the cell cycle distribution of subTADs and TADs that contain at least one subTAD based on their time of emergence. *P* values were calculated using a two-sided Fisher’s exact test (prometaphase + ana/telophase compared with early G1 + mid G1).

during later stages (Extended Data Fig. 4c). In line with subTAD merging, we observed gains in contacts across subTAD boundaries over time (Extended Data Fig. 4d). Accordingly, a substantial portion of subTAD boundaries detected at prometaphase exhibit increased insulation scores (indicative of reduced insulation), whereas for most TAD boundaries, insulation scores decrease as cells progressed from prometaphase into G1 (Extended Data Fig. 4e). Independent algorithms yielded similar trends of subTAD merging after mitosis^{8,10} (Extended Data Fig. 4f–m). Together, these analyses suggest a ‘bottom-up’ model of hierarchical domain reorganization during the prometa-to-G1 phase transition.

A loop-extrusion model has been proposed to explain the formation of TADs and chromatin loops, wherein the cohesin complex extrudes the chromatid until it encounters pairs of convergently oriented CTCF-binding sites^{11,12}. Because cell cycle dynamics of loop formation as well as CTCF and cohesin binding could inform this (or alternative) models, we surveyed the chromatin-binding profiles of CTCF and cohesin by chromatin-immunoprecipitation followed by sequencing (ChIP–seq). We generated highly concordant replicates (Extended Data Fig. 1g, h) and identified 41,699 CTCF-binding sites and 22,003 binding sites for Rad21, a cohesin subunit (Supplementary Table 2). Approximately 88.7% (19,520) of Rad21 peaks were co-occupied by CTCF. Notably, around 18.6% (7,741) of CTCF peaks are reproducibly detected in prometaphase cells, indicating that a considerable amount of CTCF remains bound to mitotic chromatin (Extended Data Fig. 5a, c, d). Previous reports have described varying degrees of CTCF mitotic retention^{13,14}. Unlike CTCF, Rad21 failed to show localized chromatin binding during prometaphase (Extended Data Fig. 5b–d). Motif scan and genomic distribution analysis failed to identify distinct features associated with CTCF peaks present in both interphase and mitosis (IM-peaks) (Extended Data Fig. 5e, f). However, IM-peaks tend to be more tissue invariant and are more likely to be co-occupied by Rad21 during interphase (Extended Data Fig. 5f). CTCF and cohesin resume chromatin occupancy after mitosis with markedly different kinetics.

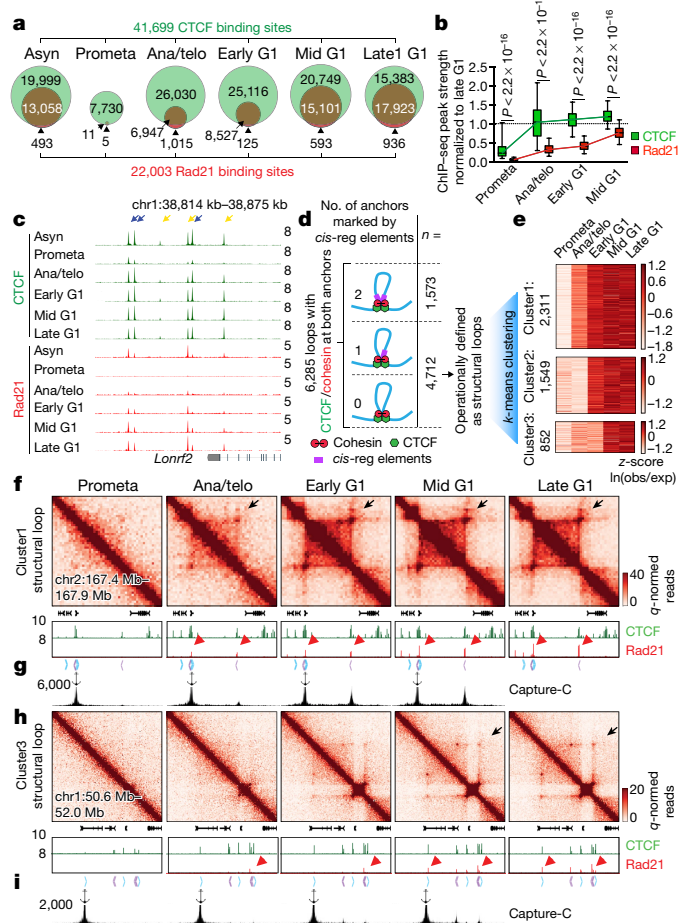


Fig. 3 | Focal accumulation of cohesin is delayed compared to that of CTCF and coincides with structural loop formation. **a**, Venn diagrams showing the distribution of CTCF and Rad21 ChIP-seq peaks across cell cycle stages. **b**, Box plots showing the recovery rate of CTCF ($n = 33,306$) and Rad21 ($n = 18,859$) peaks. Peaks absent from late G1 were omitted from the analysis. For all box plots, centre lines denote medians; box limits denote 25th–75th percentile; whiskers denote 5th–95th percentile. P values were calculated using a two-sided Mann–Whitney U -test. **c**, Genome browser tracks of CTCF and Rad21 at the *Lonrf2* locus across cell cycle stages. $n = 2–3$ biological replicates. Blue and yellow arrows indicate IM- and interphase-only (IO)-CTCF binding sites, respectively. **d**, Schematic depicting the classification of loops. All loops with CTCF/cohesin co-occupancy at both anchors were subdivided into those with 0, 1 or 2 anchors marked by *cis*-regulatory elements. Those with 0 or 1 were operationally defined as structural loops. **e**, Heat map showing the result of k -means clustering on the 4,712 structural loops. **f**, Hi-C contact maps showing a representative region that contains a cluster 1 structural loop (chr2: 167.4 Mb–167.9 Mb, black arrows), along with genome browser tracks of CTCF and Rad21 ChIP-seq profiles. Rad21 peaks at two loop anchors are indicated by red arrowheads. Chevron arrows highlight positions and orientations of CTCF sites at the loop anchors. Bin size, 10 kb. **g**, Capture-C interaction profile of the same region as shown in **f**. $n = 3$ biological replicates. The anchor symbol shows position of the capture probe. **h**, **i**, similar to **f**, **g**, showing a representative region that contains a cluster 3 (slowly emerging) structural loop (chr1: 50.6 Mb–52.0 Mb, black arrows).

The majority of CTCF peaks are immediately restored in ana/telophase, whereas Rad21 peaks appear much more gradually (Fig. 3a–c; Extended Data Fig. 5g–i). Delayed nuclear import as well as chromatin loading and/or movement along the chromatid could account for the slow focal accumulation of cohesin after mitosis. We performed live-cell imaging on asynchronous G1E-ER4 cells that endogenously express mCherry-tagged CTCF or mCherry-tagged SMC3 (a cohesin subunit)

(Extended Data Fig. 5j). Consistent with the ChIP-seq data and a previous report¹⁵, CTCF rapidly accumulates on telophase chromosomes, whereas SMC3 is excluded from chromosomes during metaphase, telophase and cytokinesis (Extended Data Fig. 5k). Moreover, after G1 entry, nuclear import of SMC3 is also slower compared to that of CTCF (Extended Data Fig. 5k, l). These results suggest that the delayed kinetics of focal cohesin accumulation might be a composite of nuclear import, association with chromatin, and migration along the chromatid.

The transient decoupling of cohesin from CTCF during mitotic exit offers the opportunity to separately assess their roles in post-mitotic loop formation. Using a modified HICCUPS algorithm we identified 13,317 chromatin loops, progressively gained from prometaphase to late G1, with highly concordant loop strength between biological replicates (Extended Data Fig. 6a–c; Supplementary Table 3). Of these loops, 6,285 (about 47.2%) contain CTCF and cohesin co-occupied sites at both anchors (Fig. 3d). These loops were further filtered to eliminate interactions between putative *cis*-regulatory elements (for example, enhancer–promoter loops), resulting in 4,712 operationally defined ‘structural’ loops (Fig. 3d). To investigate how fast structural loops are formed we performed k -means clustering, which revealed three clusters with distinct formation dynamics (Fig. 3e). Cluster 1 loops display strong interactions in ana/telophase, whereas the formation of cluster 2 and 3 loops is delayed (Fig. 3e, f, h; Extended Data Fig. 6d, e). Analysis by Capture-C validated the differential dynamics of structural loops at two representative loci (Fig. 3g, i). Notably, anchors of cluster 1 loops show enrichment of Rad21 at ana/telophase, whereas anchors of cluster 2 and 3 loops acquire Rad21 more gradually (Fig. 3f, h; Extended Data Fig. 6d, e). By contrast, CTCF is rapidly enriched at anchors of all three loop clusters (Fig. 3f, h; Extended Data Fig. 6d, e). The strengths of structural loops are highly correlated with ChIP-seq signals of Rad21 at their anchors over time, but significantly less so with those of CTCF (Extended Data Fig. 6f). Late-occurring structural loops are significantly larger than earlier ones, suggesting a correlation between size and time to formation (Extended Data Fig. 6g). Together, our results reveal three clusters of structural loops with distinct formation dynamics, and suggest that the accumulation of cohesin—but not CTCF—is rate-limiting for the formation of structural loops after mitosis.

Stripes in the contact maps are thought to reflect interactions between a single locus and a continuum of genomic regions, and are considered as evidence for the loop extrusion model¹⁷. Using a modified statistical modelling approach¹⁷, we identified 1,775 stripes genome-wide. The majority of them contain inwardly oriented CTCF sites at their anchors (Extended Data Fig. 7a). Notably, these striped contacts grow directionally over time but display punctuated enrichment at select CTCF sites (Extended Data Fig. 7b, d). This is consistent with an extrusion mechanism in which some CTCF-binding sites serve as obstacles to cohesin processivity. We also observed blockage of stripe extension that correlates with the presence of strong CTCF-binding sites, resulting in the formation of structural loops at the far end of the stripes (Extended Data Fig. 7b). Together, our data are consistent with dynamic loop extrusion after mitosis. Stripe-like patterns that appear rapidly with little or no further growth were also observed, and are discussed below (Extended Data Fig. 7c, e, f).

Next we investigated interactions between *cis*-regulatory elements. We identified 3,812 chromatin loops with both anchors marked by promoters or putative enhancers, which we termed E/P loops (Fig. 4a). This number is probably an underestimate because short range E/P loops can escape detection. Notably, a considerable portion (approximately 58.7%, 2,239) of E/P loops have only one or no anchor that co-localizes with CTCF and cohesin co-occupied sites, suggesting that E/P loops may form by a mechanism other than CTCF/cohesin-mediated loop extrusion (Fig. 4a). These seemingly CTCF/cohesin independent E/P loops are intensified significantly faster than structural loops (Fig. 4b, Extended Data Fig. 6h). Note that the faster formation of E/P loops compared to structural loops is not explained by differences in loop

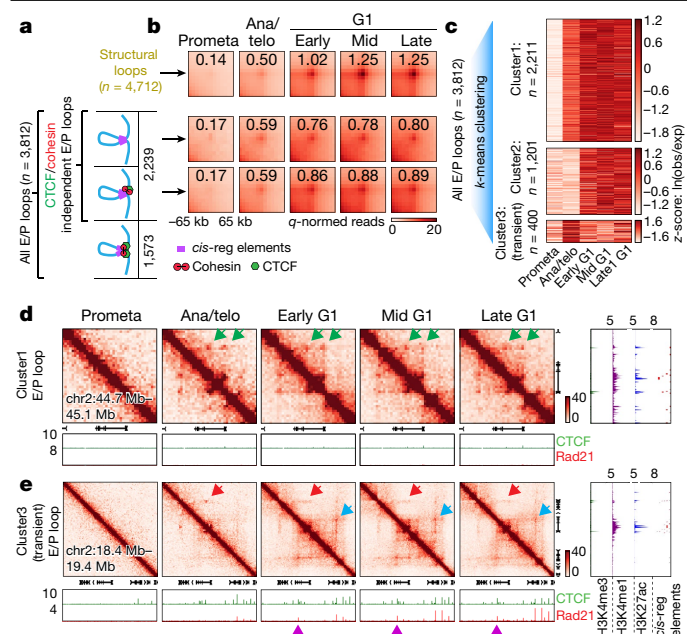


Fig. 4 | *cis*-Regulatory contacts are established rapidly after mitosis and can be transient. **a**, Schematic depicting the classification of loops. E/P loops were subdivided into those with 0, 1 or 2 anchors containing CTCF/cohesin-occupied sites. Those with 0 or 1 anchor co-occupied by CTCF/cohesin were classified as E/P loops independent from CTCF and cohesin. **b**, Aggregated peak analysis of CTCF/cohesin independent E/P loops (middle and bottom) in comparison to structural loops (top). Bin size, 10 kb. Numbers indicate average loop strength: $\ln(\text{observed}/\text{expected})$. **c**, Heat map of *k*-means clustered E/P loops. **d**, Hi-C contact maps of a representative region (chr2: 44.7 Mb–45.1 Mb) containing cluster 1 E/P loops (green arrows), coupled with browser tracks of CTCF and Rad21 occupancy. Bin size, 10 kb. The colour bar denotes *q*-normed reads. Tracks of H3K4me3, H3K4me1, H3K27ac and annotations of *cis*-regulatory elements were from asynchronously growing G1E-ER4 cells. **e**, Similar to **d**, a representative region (*Commd3* locus, chr2: 18.4 Mb–19.4 Mb) containing a cluster 3 (transient) E/P loop (red arrows). Blue arrows denote the formation of a downstream, potentially interfering structural loop. Purple arrowheads indicate CTCF/cohesin binding at the potentially interfering structural loop anchor.

size (Extended Data Fig. 6i). Accordingly, among loops established in ana/telophase, about 69.3% are E/P loops whereas only 11.6% are structural loops (Extended Data Fig. 6j). These trends are reversed in mid G1 (18.4% E/P and 42.3% structural loops, respectively). Hence, E/P loops may not require CTCF and cohesin, and can be rebuilt faster than structural loops after mitosis.

Clustering all E/P loops on the basis of their time of enrichment yielded at least three classes with distinct post-mitotic formation kinetics. Cluster 1 (2,211, 58%) E/P contacts are rapidly enriched in ana/telophase, whereas cluster 2 contacts (1,201, 31.5%) form in early G1 (Fig. 4c, d; Extended Data Fig. 8a, b). We also discovered a third cluster (400, 10.5%) of E/P loops that peak early in ana/telophase and gradually diminish in G1 (Fig. 4c, e; Extended Data Fig. 8c, d, f). We independently validated this transient nature between certain *cis*-regulatory elements by Capture-C at the two manually identified loci *Pde12* and *Morc3* (Extended Data Fig. 8c, e). In an effort to understand the mechanisms that underlie this subset of transient E/P loops, we noticed that approximately 55% of them span either a boundary or an anchor of a nearby structural loop that is established later in G1 (Fig. 4e, Extended Data Fig. 8c). Moreover, these boundaries and loop anchors within cluster 3 E/P loops display more substantial insulation compared to those within clusters 1 or 2 (Extended Data Fig. 8g). We therefore speculate that emerging boundaries or nearby structural loops may interfere with E/P loops (Extended Data Fig. 1a). To test this hypothesis, we set out to assay cluster 3 E/P loop dynamics after perturbing the nearby structural

loop. We focused on the interaction between the *Commd3* promoter and a distal *cis*-regulatory element. We deleted the CTCF core motif of a potential interfering structural loop anchor, resulting in the abrogation of CTCF and Rad21 binding (Extended Data Fig. 8f, h, i). Notably, in the mutant cells, interactions between the *Commd3* promoter and the distal *cis*-regulatory element are prolonged after mitosis, compared to controls (Extended Data Fig. 8j–l). These results provide a precedent for a dynamic interplay between structural and E/P loops. However, insulation between regulatory elements is unlikely to fully explain the transient nature of cluster 3 E/P loops, because only around 55% of them span boundaries or interfering loop anchors. Additional mechanisms, such as competition between regulatory elements, may also contribute to the transient nature of cluster 3 E/P loops. In summary, we identified a special class of transient E/P contacts after mitosis, which may in some cases be broken by CTCF and cohesin.

To explore the relationship between chromatin organization and transcription activation¹⁸ after mitosis, we carried out Pol II ChIP-seq¹⁹ (Extended Data Fig. 1i). Transcription is largely silenced in prometaphase, but rapidly reinitiates in ana/telophase and positively correlates with A-type compartments (Extended Data Fig. 9a, b). Collectively, we identified 7,535 active genes after mitosis (Supplementary Table 4). Genes display comparable reactivation dynamics regardless of whether they are located in domains called at early or later stages of the cell cycle, suggesting that domain formation may exert only limited influence on gene reactivation after mitosis (Extended Data Fig. 9c). We then stratified active genes on the basis of their Pol II occupancy over time through principal component analysis¹⁹. In a previous study we observed that a large fraction of genes acquires strong Pol II occupancy early after mitosis, followed by a reduction in signal intensity. This ‘spike’ in gene reactivation manifests as the first principal component (PC1) and separates ‘spiking’ genes from late-activating genes¹⁹. Similarly, the current data recapitulate this transient hyperactivation as represented by PC1 (Extended Data Fig. 9d–f). To examine the relationship between gene spiking and E/P loop formation, we began by stratifying all active genes on the basis of whether or not they are positioned at E/P loop anchors (Extended Data Fig. 9g, h). In general, formation of E/P loops is positively correlated with Pol II occupancy over time (median Pearson $r \approx 0.65$). Additionally, we found that genes at cluster 3 E/P loops are more likely to display post-mitotic transcriptional spiking compared to those at cluster 1 or 2 loops, or those with no detectable E/P loops (Extended Data Fig. 9i, j). Regarding genes associated with cluster 1 or 2 E/P loops, activation was also positively correlated with loop strength over time (median Pearson $r \approx 0.67$). These results suggest that transient E/P loops may contribute to post-mitotic gene spiking. However, a caveat to this interpretation is that a much larger number of genes spike than are associated with transient E/P loops. This suggests that E/P contacts cannot be solely responsible for spiking in post-mitotic transcription. Nonetheless, although the causal relationship between gene spiking and transient E/P loops remains uncertain, the overall positive correlation between E/P loop strength and Pol II occupancy over time suggests a potential role of E/P contacts in transcription after mitosis.

We exploited the natural transition from a relatively unorganized state (prometaphase) into fully established chromatin organization late in G1 to interrogate mechanisms by which chromatin is hierarchically organized (Extended Data Fig. 1a). We showed that A/B compartmentalization was disrupted in prometaphase despite histone marks being largely maintained²⁰. We also show that local (around 10 Mb) compartmentalization of chromatin initiates rapidly after mitosis, and continues to expand and increase in strength. Study of the cell cycle dynamics of chromatin also enabled the testing of predictions made by the loop extrusion model. First, small TADs and structural loops are formed more quickly than larger ones. Second, stripes in the contact maps increase in length over time. Third, based on the kinetics of CTCF and cohesin deposition on chromatin, it is clear that CTCF does not form detectable loops without cohesin even though it can form

multimers²¹. However, it is possible that CTCF pairs with itself—or with other factors such as YY1^{22,23}—to facilitate the establishment of contacts among *cis*-regulatory elements, such as those observed at early time points independently of cohesin.

Our integrative analysis of loops and histone-modification profiles reveals a group of E/P loops that can be independent from CTCF and cohesin co-binding. A distinctive feature of E/P loops is their fast appearance compared to structural loops. It is possible that E/P contacts form via collisions of chromatin regions with similar epigenetic states. This is supported by our observation that their post-mitotic recovery rate positively correlates with the intensity of active histone marks at anchors (Extended Data Fig. 8m). It is noteworthy that 16.4% of stripe-like structures that lack inwardly oriented CTCF display only little or no further growth during G1 phase and are highly enriched for histone H3 Lys27 acetylation at their anchors (Extended Data Fig. 7c, e, f). Loop extrusion is unlikely to account for these types of stripe-shaped contact. Instead, these contacts might represent small compartments, defined by local enrichment of transcription factors and chromatin modifications²⁴. Similarly, transient E/P loops might result from less discriminatory affinity among regions with similar chromatin states. In summary, our findings describe a dynamic hierarchical framework of post-mitotic chromatin configuration that supports a bottom-up model for the formation of contact domains, implicates CTCF and cohesin in post-mitotic loop extrusion, and identifies extrusion independent pathways that lead to compartmentalization and contacts of *cis*-regulatory networks.

Online content

Any methods, additional references, Nature Research reporting summaries, source data, extended data, supplementary information, acknowledgements, peer review information; details of author contributions and competing interests; and statements of data and code availability are available at <https://doi.org/10.1038/s41586-019-1778-y>.

1. Naumova, N. et al. Organization of the mitotic chromosome. *Science* **342**, 948–953 (2013).
2. Gibcus, J. H. et al. A pathway for mitotic chromosome formation. *Science* **359**, eaao6135 (2018).
3. Nagano, T. et al. Cell-cycle dynamics of chromosomal organization at single-cell resolution. *Nature* **547**, 61–67 (2017).

4. Rao, S. S. P. et al. A 3D map of the human genome at kilobase resolution reveals principles of chromatin looping. *Cell* **159**, 1665–1680 (2014).
5. Weiss, M. J., Yu, C. & Orkin, S. H. Erythroid-cell-specific properties of transcription factor GATA-1 revealed by phenotypic rescue of a gene-targeted cell line. *Mol. Cell. Biol.* **17**, 1642–1651 (1997).
6. Dileep, V. et al. Topologically associating domains and their long-range contacts are established during early G1 coincident with the establishment of the replication-timing program. *Genome Res.* **25**, 1104–1113 (2015).
7. Lieberman-Aiden, E. et al. Comprehensive mapping of long-range interactions reveals folding principles of the human genome. *Science* **326**, 289–293 (2009).
8. Norton, H. K. et al. Detecting hierarchical genome folding with network modularity. *Nat. Methods* **15**, 119–122 (2018).
9. Li, B. et al. A comprehensive mouse transcriptomic bodymap across 17 tissues by RNA-seq. *Sci. Rep.* **7**, 4200 (2017).
10. Yu, W., He, B. & Tan, K. Identifying topologically associating domains and subdomains by Gaussian Mixture model And Proportion test. *Nat. Commun.* **8**, 535 (2017).
11. Sanborn, A. L. et al. Chromatin extrusion explains key features of loop and domain formation in wild-type and engineered genomes. *Proc. Natl Acad. Sci. USA* **112**, E6456–E6465 (2015).
12. Fudenberg, G. et al. Formation of chromosomal domains by loop extrusion. *Cell Reports* **15**, 2038–2049 (2016).
13. Oomen, M. E., Hansen, A. S., Liu, Y., Darzacq, X. & Dekker, J. CTCF sites display cell cycle-dependent dynamics in factor binding and nucleosome positioning. *Genome Res.* **29**, 236–249 (2019).
14. Owens, N. et al. CTCF confers local nucleosome resiliency after DNA replication and during mitosis. *eLife* **8**, e47898 (2019).
15. Cai, Y. et al. Experimental and computational framework for a dynamic protein atlas of human cell division. *Nature* **561**, 411–415 (2018).
16. Hughes, J. R. et al. Analysis of hundreds of *cis*-regulatory landscapes at high resolution in a single, high-throughput experiment. *Nat. Genet.* **46**, 205–212 (2014).
17. Vian, L. et al. The energetics and physiological impact of cohesin extrusion. *Cell* **173**, 1165–1178.e20 (2018).
18. Rowley, M. J. et al. Evolutionarily conserved principles predict 3D chromatin organization. *Mol. Cell* **67**, 837–852.e7 (2017).
19. Hsiung, C. C.-S. et al. A hyperactive transcriptional state marks genome reactivation at the mitosis-G1 transition. *Genes Dev.* **30**, 1423–1439 (2016).
20. Behera, V. et al. Interrogating histone acetylation and BRD4 as mitotic bookmarks of transcription. *Cell Rep.* **27**, 400–415.e5 (2019).
21. Yusufzai, T. M., Tagami, H., Nakatani, Y. & Felsenfeld, G. CTCF tethers an insulator to subnuclear sites, suggesting shared insulator mechanisms across species. *Mol. Cell* **13**, 291–298 (2004).
22. Weintraub, A. S. et al. YY1 is a structural regulator of enhancer–promoter loops. *Cell* **171**, 1573–1588 (2017).
23. Beagan, J. A. et al. YY1 and CTCF orchestrate a 3D chromatin looping switch during early neural lineage commitment. *Genome Res.* **27**, 1139–1152 (2017).
24. Schwarzer, W. et al. Two independent modes of chromatin organization revealed by cohesin removal. *Nature* **551**, 51–56 (2017).

Publisher's note Springer Nature remains neutral with regard to jurisdictional claims in published maps and institutional affiliations.

© The Author(s), under exclusive licence to Springer Nature Limited 2019

Article

Reporting summary

Further information on research design is available in the Nature Research Reporting Summary linked to this paper.

Data availability

All figures include publicly available data. The Hi-C, Capture-C and ChIP-seq data generated and analysed in this study are deposited in the Gene Expression Omnibus repository under accession number GSE129997 for public access. Additional external ChIP-seq data previously reported are available at: H3K27ac (GSE61349)²⁵, H3K4me1 (GSM946535)²⁶, H3K4me3 (GSM946533)²⁶, H3K36me3 (GSM946529)²⁶ and H3K9me3 (GSM946542)²⁶. CTCF peak files from 13 different tissues are available through the ENCODE project (<https://www.encode-project.org/>) with accession numbers ENCF001LFU, ENCF001LHE, ENCF001LHY, ENCF001LJL, ENCF001LKO, ENCF001LMN, ENCF001LNK, ENCF001LOR, ENCF001LPI, ENCF001LQB, ENCF001LQS, ENCF001LSE and ENCF001LSW.

Code availability

Code used in this study is available upon request from the corresponding authors.

25. Dogan, N. et al. Occupancy by key transcription factors is a more accurate predictor of enhancer activity than histone modifications or chromatin accessibility. *Epigenetics Chromatin* **8**, 16 (2015).

26. Wu, W. et al. Dynamic shifts in occupancy by TAL1 are guided by GATA factors and drive large-scale reprogramming of gene expression during hematopoiesis. *Genome Res.* **24**, 1945–1962 (2014).

Acknowledgements We thank members of the Blobel and Phillips-Cremins laboratories for discussions, E. Apostolou and J. Dekker for discussing data before publication, L. Mirny for insights, the CHOP flow core facility staff and A. Stout for expert technical support. This work was supported by grants R37DK058044 to G.A.B., R24DK106766 to G.A.B. and R.C.H., U01HL129998A to J.E.P.-C. and G.A.B., The New York Stem Cell Foundation to J.E.P.-C., the NIH Director's New Innovator Award from the National Institute of Mental Health (1DP2MH11024701; J.E.P.-C.) and a generous gift from the DiGaetano family to G.A.B. J.E.P.-C. is a New York Stem Cell Foundation (NYSCF) Robertson Investigator. We acknowledge support from the Spatial and Functional Genomics program at The Children's Hospital of Philadelphia.

Author contributions H.Z., J.E.P.-C. and G.A.B. conceived the study and designed experiments. H.Z. performed experiments with help from P.H., H.W., C.A.K., B.G. and R.C.H. D.J.E. performed initial Hi-C data pre-processing and domain calling. H.Z. performed A/B compartment and ChIP-seq related analysis with help from Y.L. T.G.G. performed loop calling, classification and clustering, and aggregated peak analysis and aggregated domain analysis. K.R.T. performed stripe calling related analysis. D.Z. contributed to Capture-C related analysis. H.Z., J.E.P.-C. and G.A.B. wrote the paper with input from all authors.

Competing interests The authors declare no competing interests.

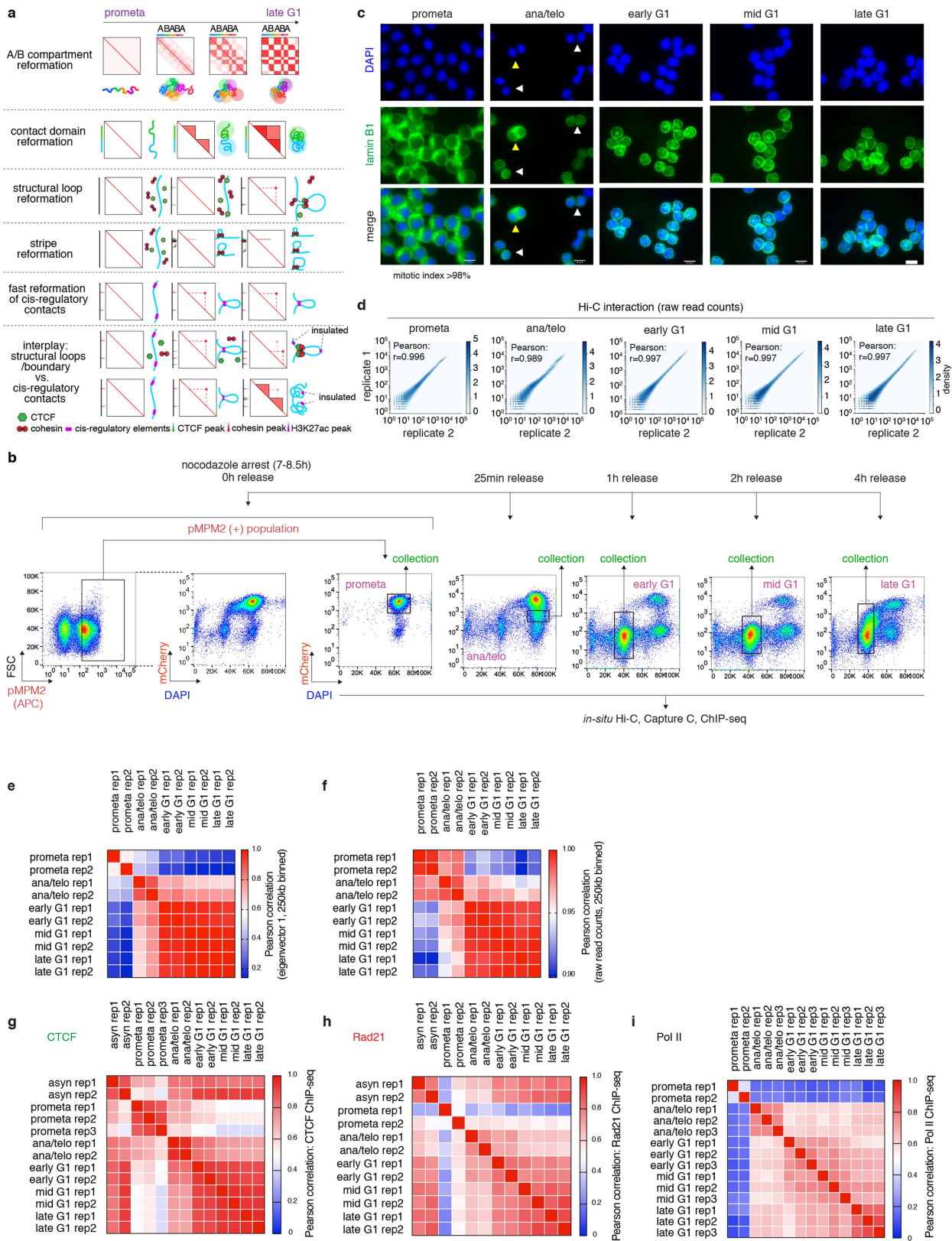
Additional information

Supplementary information is available for this paper at <https://doi.org/10.1038/s41586-019-1778-y>.

Correspondence and requests for materials should be addressed to J.E.P.-C. and G.A.B.

Peer review information *Nature* thanks David Gilbert and the other, anonymous, reviewer(s) for their contribution to the peer review of this work.

Reprints and permissions information is available at <http://www.nature.com/reprints>.



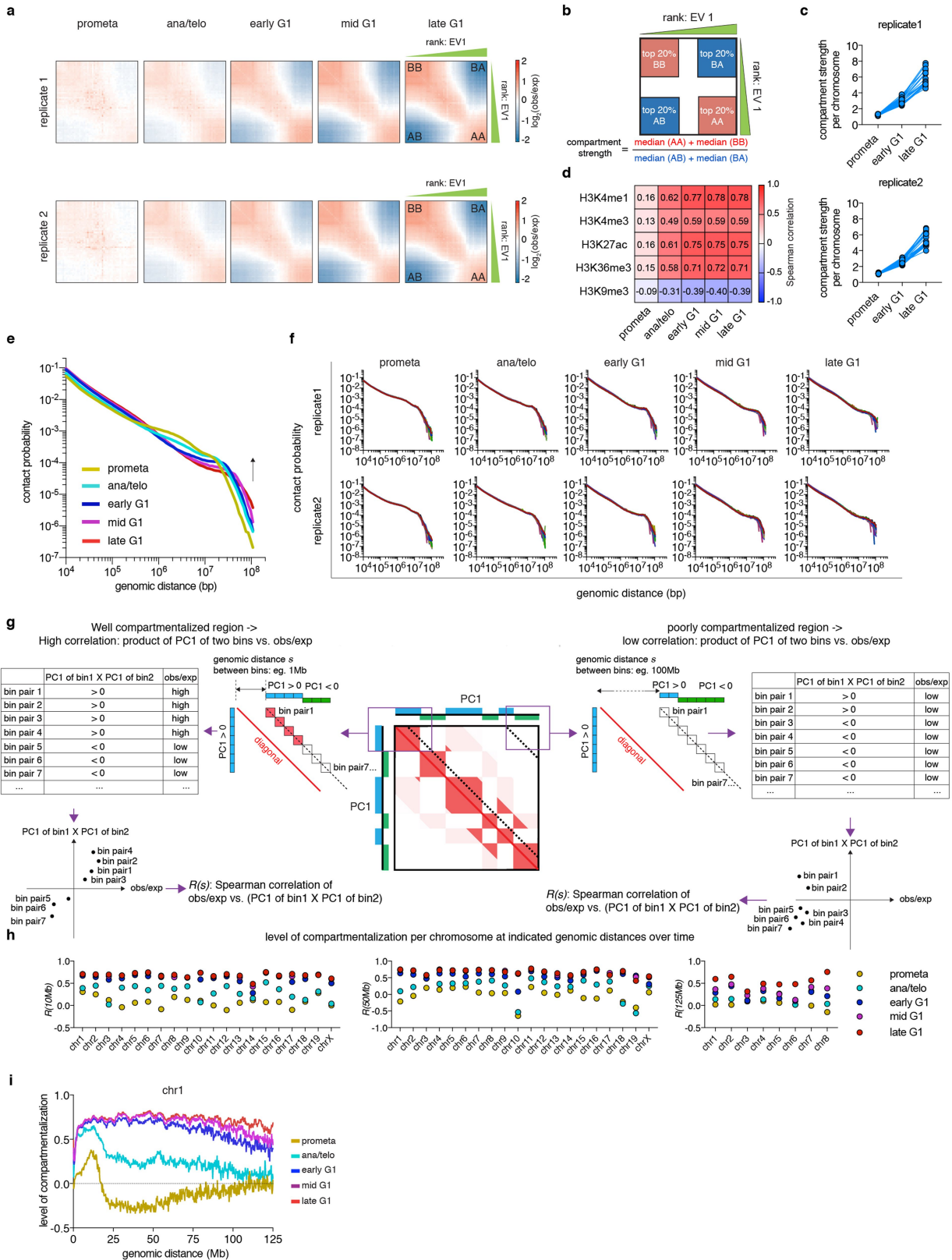
Extended Data Fig. 1 | See next page for caption.

Article

Extended Data Fig. 1 | Models, experimental workflow and data quality control.

a, From top to bottom: schematic illustration of the early emergence, gradual intensification and expansion of A/B compartments (checkerboards) from prometaphase to late G1 phase, coupled with schematics of chromatin organization; subTADs (small triangles) emerge first after mitotic exit, followed by convergence into a TAD (big triangle); formation of a structural loop coincides with the positioning of cohesin, but not CTCF after mitosis; the gradual extrusion of cohesin complex along DNA fibre from one anchor point with CTCF, reflected as enrichment of interactions between the anchor and a continuum of DNA loci on the contact map; fast formation of E/P loops after mitosis; the interplay between transient E/P loops and boundaries or structural loops. **b**, The experimental workflow. Representative flow cytometry plots showing the nocodazole arrest–release strategy based on pMPM2 (prometaphase), mCherry–MD signal, and DNA content (DAPI) staining. Similar observations were made in more than 5 independent experiments.

c, Representative images showing DAPI and lamin B1 staining of FACS-purified cells across all stages of the cell cycle. Similar observations were made in 2 independent experiments. The mitotic index of prometaphase cells after FACS purification is on average greater than 98%. Yellow and white arrowheads indicate anaphase and telophase cells, respectively. Scale bar, 10 μm . **d**, Hexbin plots showing the high correlation of Hi-C raw read counts between two biological replicates across all stages of the cell cycle. Bin size, 250 kb. **e**, Heat map showing the Pearson correlation among all Hi-C samples, based on the eigenvector 1 of 250 kb bins. **f**, Heat map showing the Pearson correlation among all Hi-C samples based on raw read counts. Bin size, 250 kb. **g–i**, Heat maps showing Pearson correlation of CTCF (**g**), Rad21 (**h**) and Pol II (**i**) ChIP–seq data among all samples. Note the overall high replicate concordance. Low correlation coefficients among replicates were only observed in samples with low signal-to-noise ratios—for example, in prometaphase.

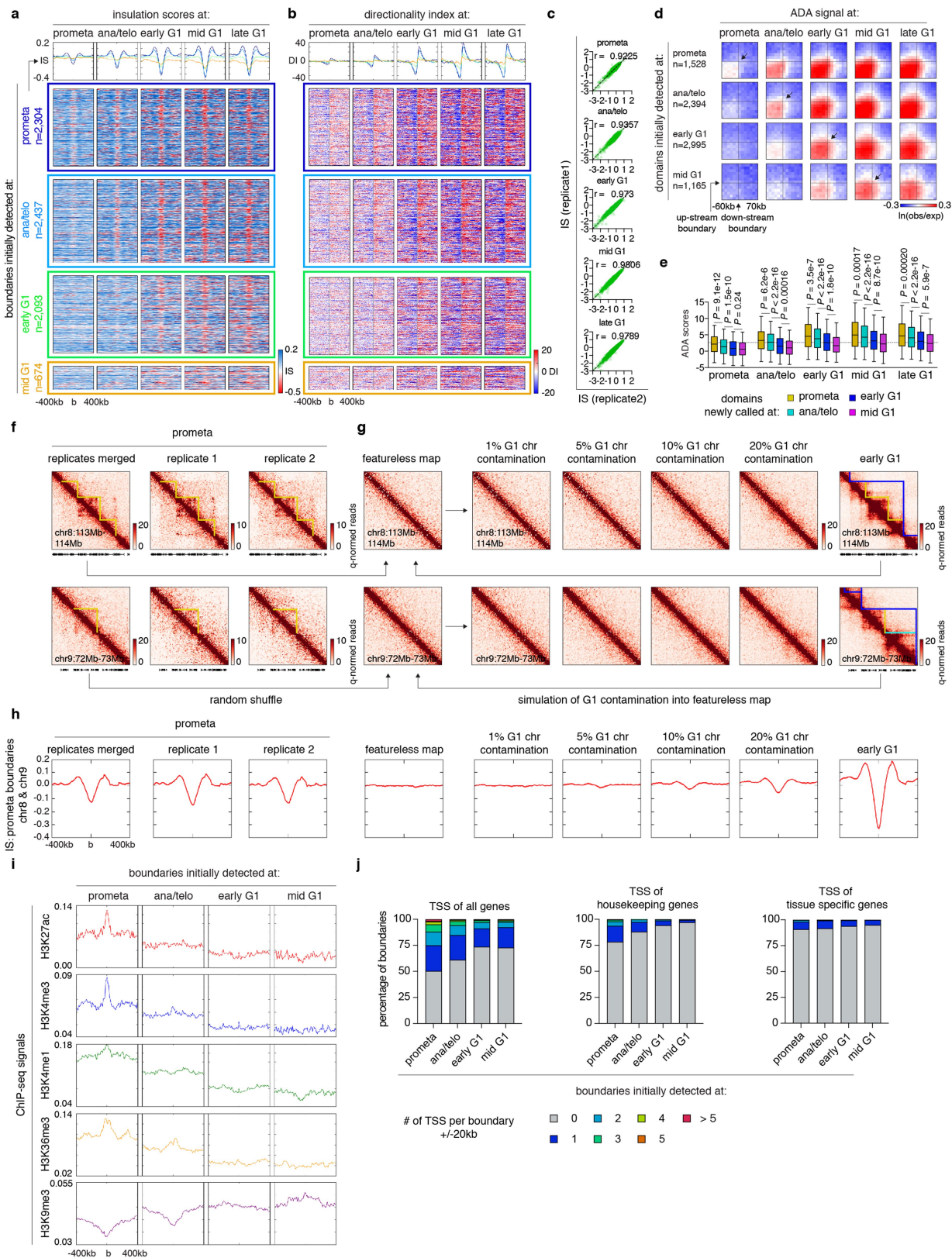


Extended Data Fig. 2 | See next page for caption.

Article

Extended Data Fig. 2 | Compartment strengthening and expansion from ana/telophase throughout late G1. **a**, Saddle plots showing the progressive gain of compartment strength over time in two biological replicates. **b**, Schematic showing the calculation of compartment strength. **c**, Line graphs showing the progressive increase of compartment strength of each individual chromosome (represented by dots) in two biological replicates. **d**, Heat map showing the genome-wide Spearman correlation coefficients between eigenvector 1 values and asynchronous-cell-derived ChIP-seq signals for the indicated histone marks. **e**, Plots of chromosome-averaged distance-dependent contact frequency ($P(s)$) at all stages of the cell cycle. **f**, $P(s)$ plots of each individual chromosome (two biological replicates). **g**, A schematic illustrating how compartmentalization levels ($R(s)$) were calculated at different

distance scales (for example, 1 Mb or 100 Mb). Each dotted line indicates a series of 250-kb bin-bin pairs that are separated by a given genomic distance s (the distance from the diagonal to the dotted line). For all bin-bin pairs separated by distance of s , a Spearman correlation coefficient $R(s)$ was generated between observed/expected and the product of two eigenvector 1 values ($PC1(\text{bin1}) \times PC1(\text{bin2})$). $R(s)$ is expected to be high in well-compartmentalized regions (left) and low at large distance scales with no compartments (right). **h**, Replicate-averaged $R(s)$ of each individual chromosome across all stages of the cell cycle when s is equal to 10, 50 and 125 Mb (only eight chromosomes were computed at the 125-Mb scale). **i**, Line graph showing the level of compartmentalization of chr1 against genomic distance at each stage of the cell cycle.

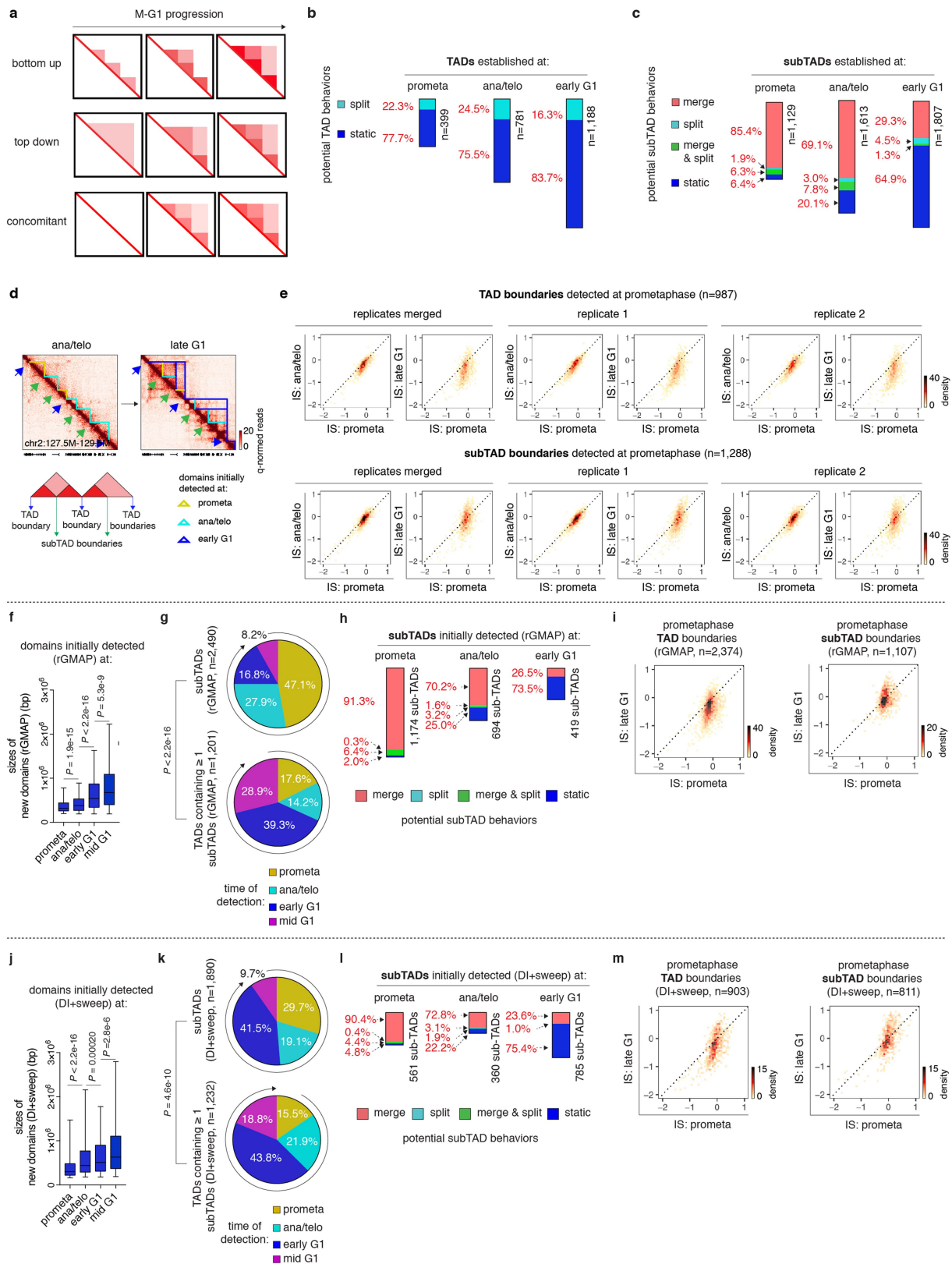


Extended Data Fig. 3 | See next page for caption.

Article

Extended Data Fig. 3 | Domain detection and residual 'domain-like' structures in prometaphase. a, b, Meta-region plots and density heat maps of insulation scores (**a**) and directionality index (**b**) centred around domain boundaries initially detected at each stage of the cell cycle. **c,** Scatter plots showing Pearson correlations of insulation scores at domain boundaries between two biological replicates. **d,** Aggregated domain analysis (ADA) of domains initially detected at each stage of the cell cycle. **e,** Box plots showing ADA scores over time for domains initially detected at prometaphase ($n = 1,360$), ana/telophase ($n = 2,260$), early G1 ($n = 2,875$) and mid G1 ($n = 1,112$). For all box plots, centre lines denote medians; box limits denote 25th–75th percentile; whiskers denote 5th–95th percentile. *P* values were calculated using a two-sided Mann–Whitney *U*-test. The dotted line indicates the average ADA score of initial domain detection. **f,** Hi-C contact maps of two representative

regions (chr8: 113 Mb–114 Mb and chr9: 72 Mb–73 Mb) showing residual domain- and boundary-like structures (yellow lines) in prometaphase in merged and individual biological replicates. Bin size, 10 kb. **g,** Simulated featureless, per cent 'G1 contaminated', and early G1 contact maps of the same regions as in **f**. Bin size, 10 kb. **h,** Meta-region plots showing the insulation scores of prometaphase, simulated featureless, 'G1-contaminated' and early G1 samples, centred around prometaphase boundaries in chr8 and chr9. **i,** Meta-region plots showing indicated histone modification profiles centred around boundaries newly detected at each stage of the cell cycle. **j,** Bar graphs showing the enrichment of transcription start sites (overall, housekeeping and tissue-specific⁹) within ± 20 kb of boundaries newly detected at each stage of the cell cycle.



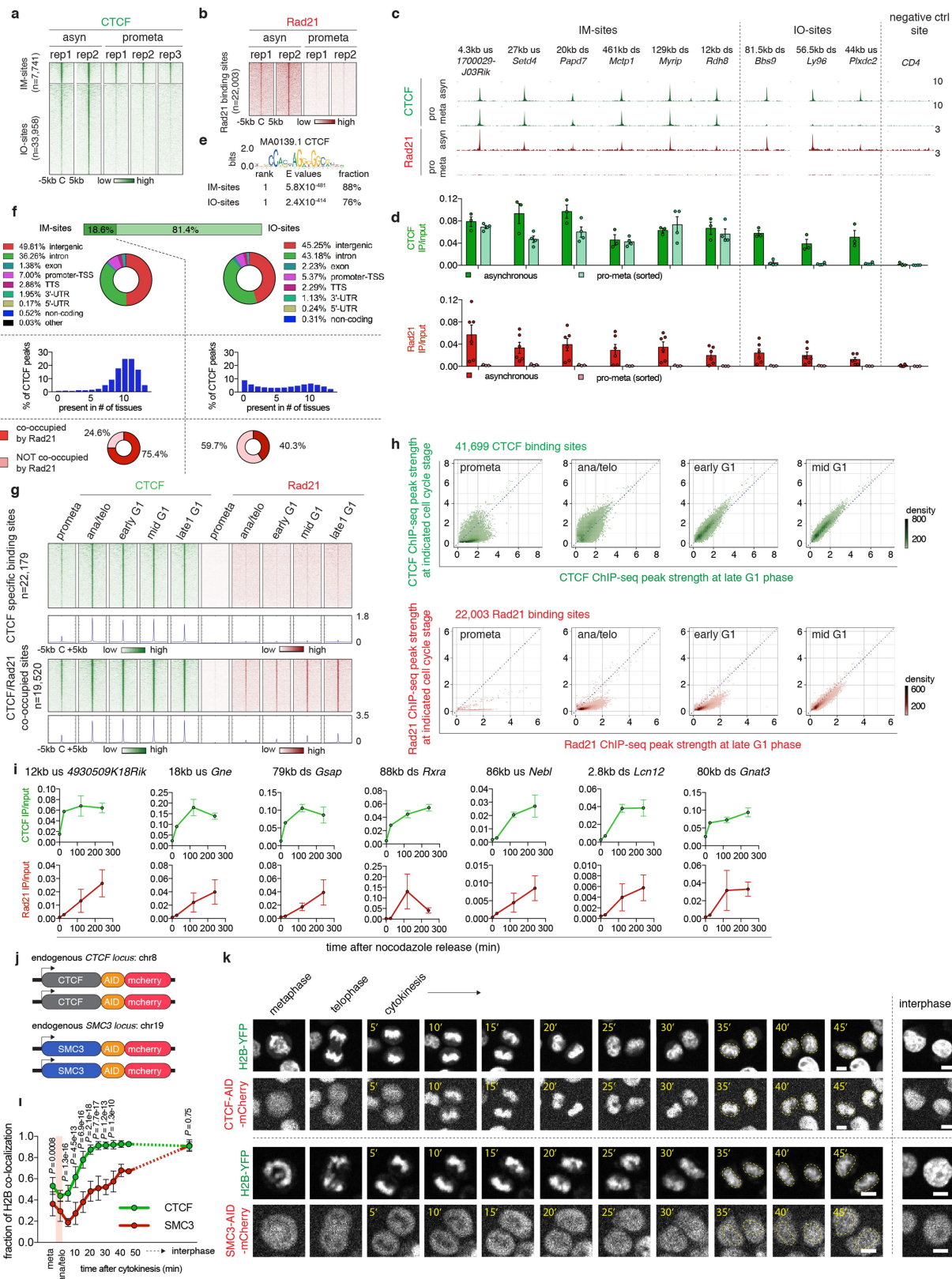
Extended Data Fig. 4 | See next page for caption.

Article

Extended Data Fig. 4 | Dynamics of TAD and subTAD after mitosis.

a, Schematic of possible models of hierarchical domain formation: bottom-up (merge), top-down (split) and concomitant. **b**, Bar graphs showing the fraction of TADs that display either type of behaviour after detection. **c**, Bar graphs showing the fraction of subTADs that display each of the four potential behaviours after detection: merge, split, merge and split, and static. **d**, Bottom, schematic showing partitioning of boundaries into TAD and subTAD boundaries. Top, Hi-C contact maps showing the change in insulation of representative TAD and subTAD boundaries from ana/telophase to late G1. SubTAD and TAD boundaries are indicated by green and blue arrows, respectively. Bin size, 10 kb. **e**, Bin plots showing the change in insulation score over time of TAD boundaries (top) and subTAD boundaries (bottom) that are detected at prometaphase in merged replicates and in two biological replicates. **f**, Box plots showing sizes of domains initially detected at prometaphase ($n=2,494$), ana/telophase ($n=1,699$), early G1 ($n=1,357$) and mid G1 ($n=682$) by rGMAP. For all box plots, centre lines denote medians; box limits

denote 25th–75th percentile; whiskers denote 5th–95th percentile. *P* values were calculated using a two-sided Mann–Whitney *U*-test. **g**, Pie charts of the cell cycle distribution of subTADs and TADs that contain at least 1 subTAD based on their time of emergence (called by rGMAP). The *P* value was calculated using a two-sided Fisher's exact test (prometaphase + ana/telophase compared with early G1 + mid G1). **h**, Bar graphs showing the fraction of subTADs detected by rGMAP that display each of the four potential behaviours after detection: merge, split, merge and split, and static. **i**, Bin plots showing the change in insulation score of TAD boundaries (left) and subTAD boundaries (right) that are detected by rGMAP at prometaphase. **j**, Box plots showing the sizes of domains initially detected at prometaphase ($n=1,105$), ana/telophase ($n=1,124$), early G1 ($n=2,385$) and mid G1 ($n=520$) by DI+sweep (directionality index + window size adjustment). For all box plots, centre lines denote medians; box limits denote 25th–75th percentile; whiskers denote 5th–95th percentile. *P* values were calculated by two-sided Mann–Whitney *U*-test. **k–m**, Similar to **g–i**, showing analyses based on domains called by DI+sweep.



Extended Data Fig. 5 | See next page for caption.

Article

Extended Data Fig. 5 | CTCF and cohesin chromatin occupancy in mitosis and G1 entry. **a**, A density heat map of CTCF ChIP-seq data of each biological replicate of asynchronous and prometaphase samples, centred around IM- and IO-CTCF binding sites. **b**, A density heat map of Rad21 ChIP-seq data of both biological replicates of asynchronous and prometaphase samples centred around all Rad21 peaks. **c**, Genome browser tracks showing CTCF and Rad21 ChIP-seq signals of asynchronous and prometaphase samples at indicated regions. $n=2-3$ biological replicates. **d**, ChIP-qPCR data of CTCF and Rad21 in asynchronous ($n=3$, 6 biological replicates for CTCF and Rad21, respectively) and prometaphase samples ($n=4$, 3 biological replicates for CTCF and Rad21, respectively). Data are mean \pm s.e.m. **e**, Motif enrichment analysis of IM- and IO-CTCF binding sites with indicated *E* values as determined by MEME-ChIP. **f**, Top, donut charts showing the genome-wide distribution of IM- and IO-CTCF binding sites. Middle, bar graphs showing the percentage of IM- or IO-CTCF binding sites that are found in indicated numbers of tissues. Bottom, donut pie chart showing the fraction of IM- and IO-CTCF binding sites that are co-occupied by Rad21. **g**, Density heat maps and meta-region plots of CTCF and

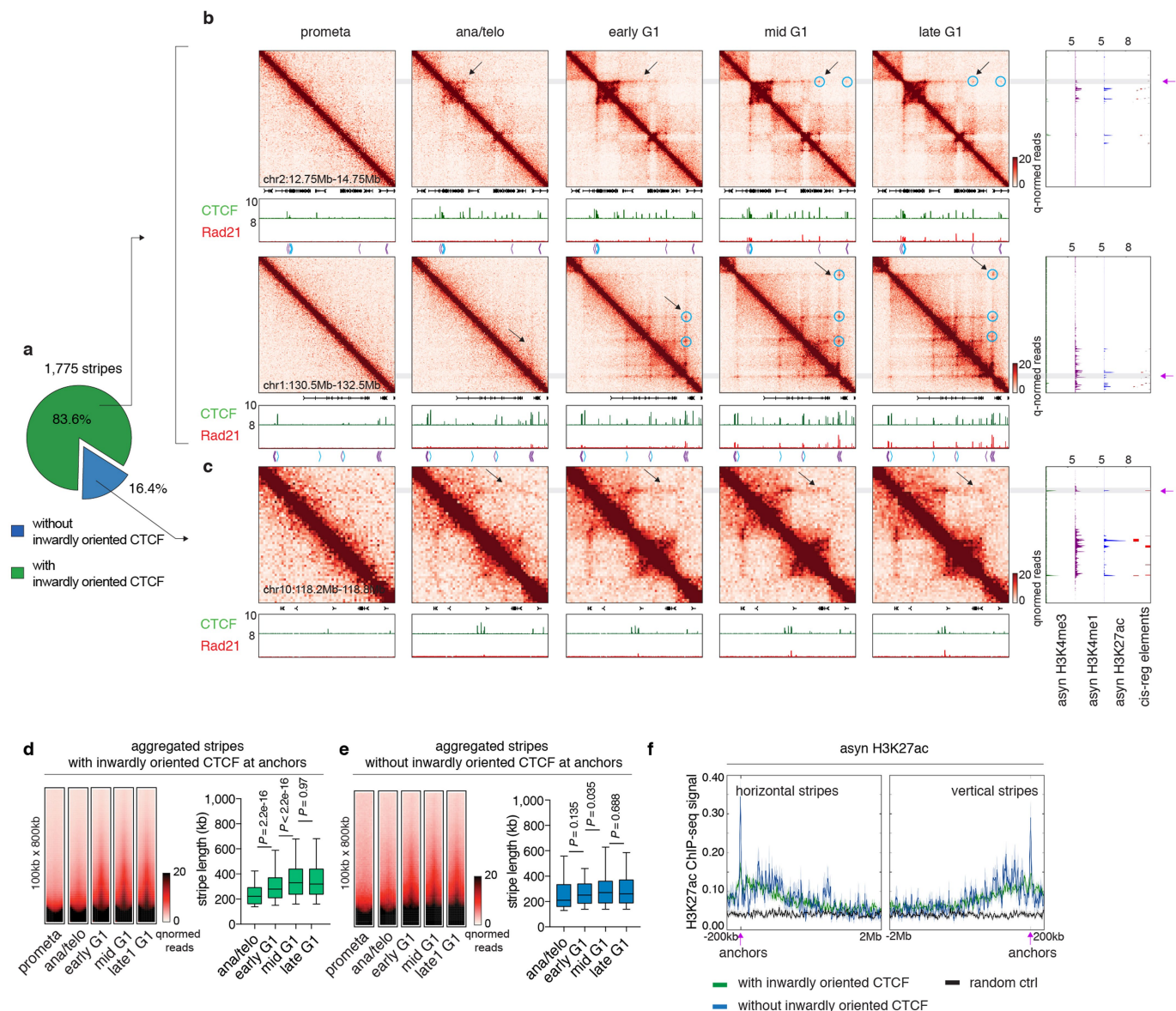
Rad21 ChIP-seq data across all time points centred around CTCF-specific and CTCF/Rad21 co-occupied binding sites. **h**, Bin plots showing ChIP-seq signals of CTCF and Rad21 peaks for each stage of the cell cycle (y axis) against late G1 (x axis). **i**, ChIP-qPCR of CTCF and Rad21 at indicated binding sites over time. $n=2$ biological replicates for 0 and 25 min, and $n=3$ biological replicates for 120 and 240 min after nocodazole release. Data are mean \pm s.e.m. **j**, Schematic showing mCherry-tagging of endogenous CTCF and SMC3. **k**, Representative images (from at least 10 dividing cells) illustrating the behaviour of mCherry-tagged CTCF and SMC3 during mitosis-early G1 phase progression. Similar observations were made in 2 independent experiments. Yellow dotted circles demarcate cell nuclei after mitosis. Scale bar, 5 μ m. **l**, Average recovery curve of mCherry-tagged CTCF and SMC3 that co-localize with H2B-YFP. Cells (11 mother cells/22 daughter cells and 10 mother cells/18 daughter cells) were analysed for CTCF and SMC3, respectively. *P* values were calculated using a two-sided Student's *t*-test. Data are mean \pm s.e.m. *P* values were omitted at time points with fewer than 5 cells.

Article

Extended Data Fig. 6 | Loop statistics and *k*-means clustering on structural loops.

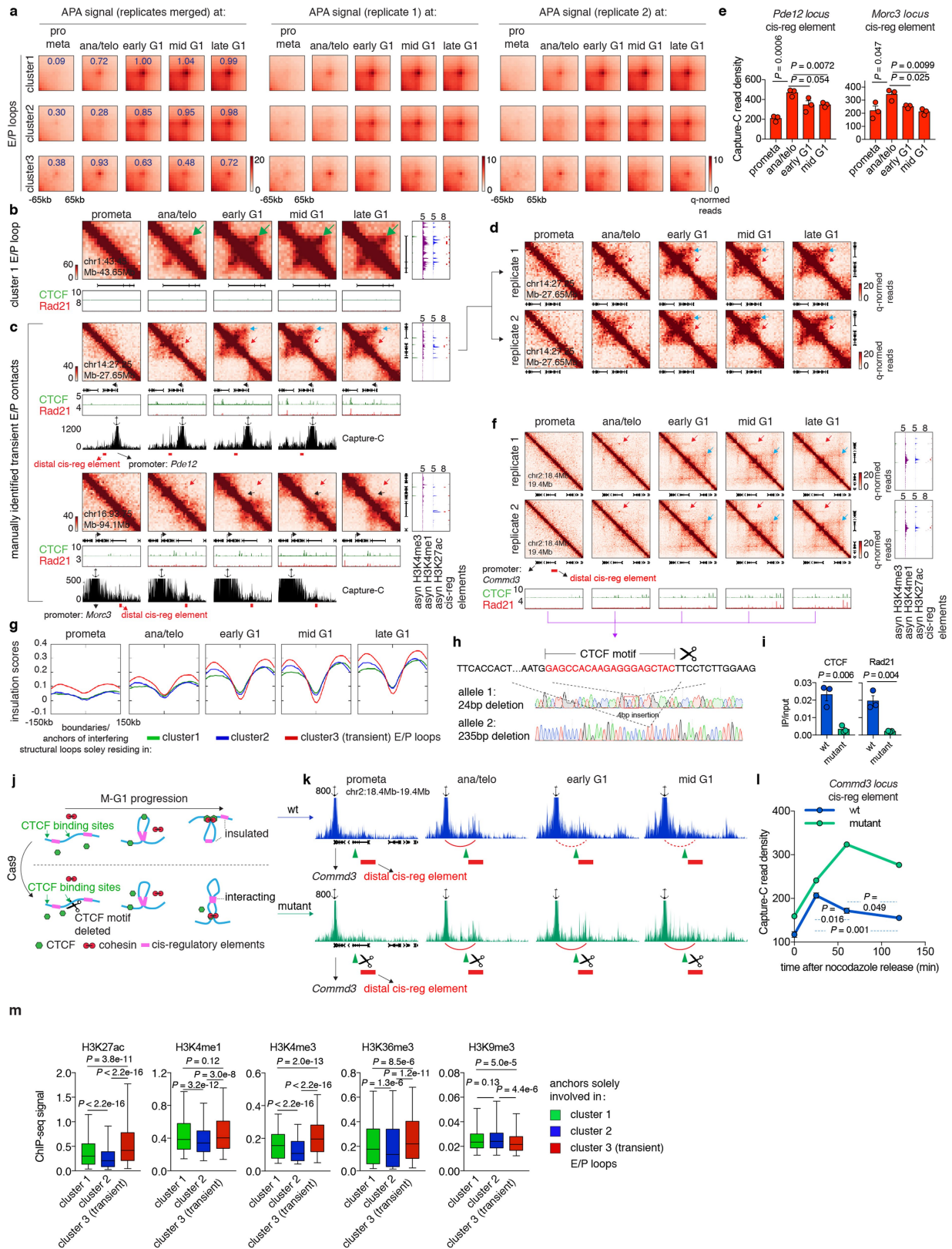
a, Bar graph showing the number of loop calls at each stage of the cell cycle. **b**, Aggregated peak analysis (APA) of loops initially detected at each stage of the cell cycle. Bin size, 10 kb. Numbers indicate average loop strength: $\ln(\text{obs}/\text{exp})$. **c**, Scatter plots showing the Pearson correlation of loop strength (read counts) between two biological replicates. **d**, Hi-C contact maps showing representative regions that contain cluster 1 (chr1: 172.8 Mb–173 Mb), 2 (chr1: 90.2 Mb–90.8 Mb) and 3 (chr2: 47.5 Mb–49 Mb) structural loops in merged and both biological replicates. Bin size, 10 kb. Loop signal enrichment is indicated by black arrows. Contact maps are coupled with genome browser tracks showing CTCF and cohesin occupancy across all stages of the cell cycle. Chevron arrows mark orientations of CTCF sites at loop anchors. **e**, APA of cluster 1, 2 and 3 structural loops across all stages of the cell cycle. Each heat map is coupled with four meta-region plots corresponding to CTCF and Rad21 ChIP-seq signals centred around either upstream or downstream loop anchors. Bin size, 10 kb. Numbers indicate average loop strength: $\ln(\text{obs}/\text{exp})$. **f**, Left and right, schematics showing how correlations are computed between CTCF or Rad21 and loop strength over time. Middle, box plot showing the Pearson correlation coefficients between CTCF or Rad21 ChIP-seq peak strength at upstream or downstream anchors and structural loop strength over time ($n = 4,712$). For all box plots, centre lines denote medians; box limits denote 25th–75th percentile; whiskers denote 5th–95th percentile. *P* values

were calculated using a two-sided Wilcoxon signed-rank test. **g**, Box plot showing sizes of structural loops initially detected at ana/telophase ($n = 90$), early G1 ($n = 2,233$), mid G1 ($n = 1,595$) and late G1 ($n = 793$). For all box plots, centre lines denote medians; box limits denote 25th–75th percentile; whiskers denote 5th–95th percentile. *P* values were calculated using a two-sided Mann–Whitney *U*-test. **h**, Average recovery curves of structural loops ($n = 4,241$) and E/P loops with 0 ($n = 678$) or 1 ($n = 1,338$) anchor co-occupied by CTCF/cohesin. The 10% of loops with the smallest increment from prometaphase to late G1 were filtered out from the analysis. Data are mean \pm 99% confidence interval. **** and ####, $P < 2.2 \times 10^{-16}$ (structural loops compared with E/P loops with 0 or 1 anchor co-occupied by CTCF/cohesin, respectively). Two-sided Mann–Whitney *U*-test. **i**, Left, average recovery curves of randomly sampled and size-matched structural loops and CTCF/cohesin independent E/P loops ($n = 2,869$ for both groups). The 10% of loops with the smallest increment from prometaphase to late G1 were filtered out from the analysis. Data are mean \pm 99% confidence interval. *P* values were calculated using a two-sided Mann–Whitney *U*-test. Right, box plot showing the comparable size distribution of these two randomly sampled groups ($n = 2,869$ for both). For both box plots, centre lines denote medians; box limits denote 25th–75th percentile; whiskers denote 5th–95th percentile. **j**, Bar graphs depicting the composition of loops newly called at each stage of the cell cycle.



Extended Data Fig. 7 | Reformation of chromatin stripes after mitosis. a, Pie chart showing the fraction of stripes with inwardly oriented CTCF at stripe anchors. **b**, Hi-C contact maps of two representative regions (chr2: 12.75 Mb–14.75 Mb and chr1: 130.5 Mb–132.5 Mb) that contain stripes with inwardly oriented CTCF. Bin size, 10 kb. Contact maps are coupled with genome browser tracks of CTCF and Rad21 across all stages of the cell cycle and tracks of asynchronous H3K4me3, H3K4me1 and H3K27ac and annotation of cis-regulatory elements. Chevron arrows mark positions and orientations of CTCF peaks at stripe and loop anchors. Lengthening of stripes is indicated by black arrows. Stripe anchors are indicated by purple arrows. Loops along the stripe axis and at the far end of stripes are indicated by blue circles. **c**, similar to **b**, Hi-C contact maps showing a representative stripe (chr10: 118.2 Mb–118.8 Mb) that

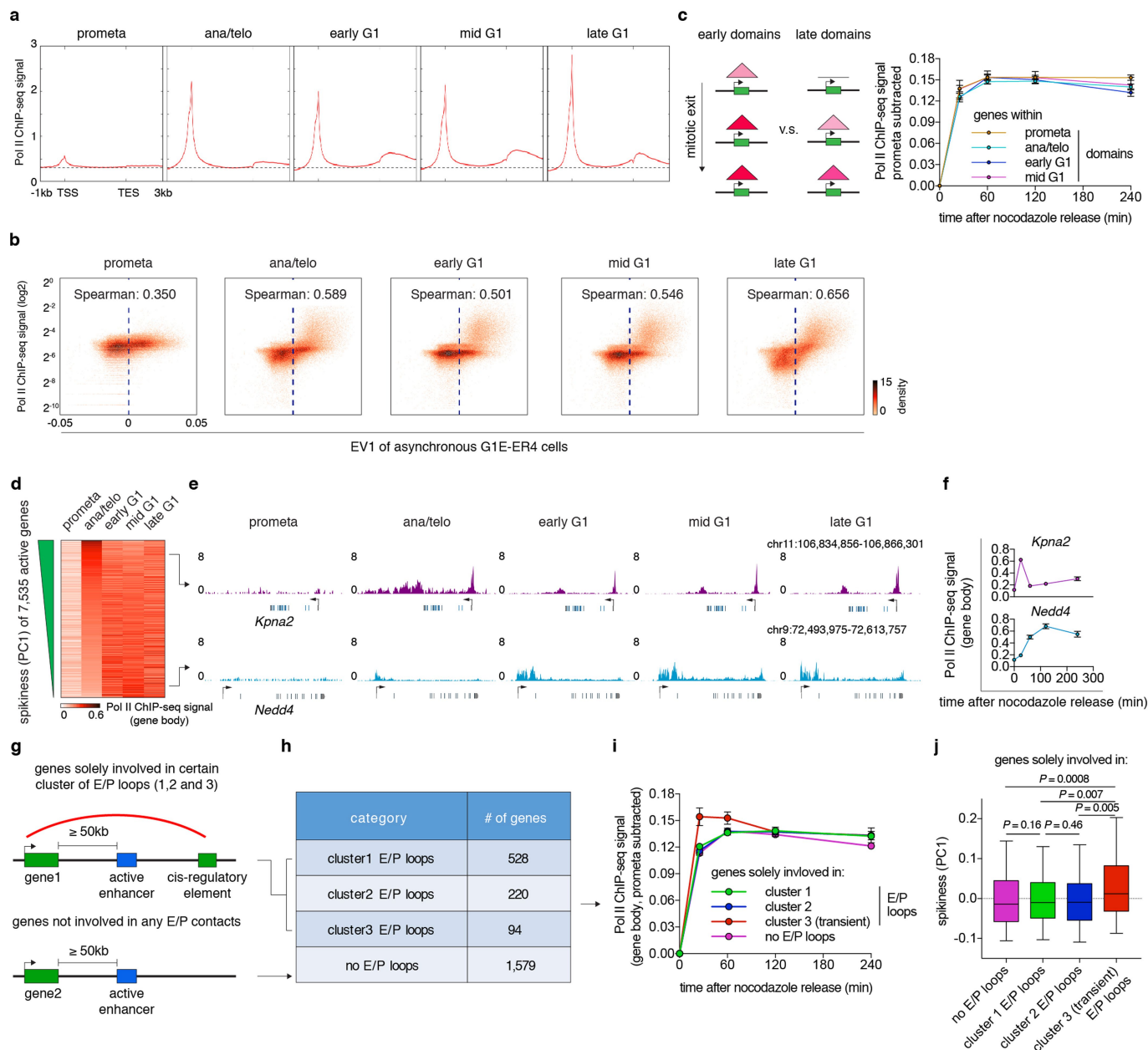
does not have inwardly oriented CTCF at the stripe anchor. **d**, Left, aggregated Hi-C contact maps that compile all stripes with inwardly oriented CTCF to show their overall dynamic growth after mitosis. Right, box plots showing the lengths of these stripes at ana/telophase ($n = 235$), early G1 ($n = 1,472$), mid G1 ($n = 1,477$) and late G1 ($n = 1,473$). For all box plots, centre lines denote medians; box limits denote 25th–75th percentile; whiskers denote 5th–95th percentile. P values were calculated using a two-sided Mann–Whitney U -test. **e**, Similar to **d**, showing stripes without inwardly oriented CTCF. $n = 72, 281, 277, 272$ for ana/telophase, early G1, mid G1 and late G1, respectively. **f**, H3K27ac ChIP-seq profile from asynchronous G1E-ER4 cells is plotted -200 kb to 2 Mb around the horizontal stripe anchors and -2 Mb to 200 kb around the vertical stripe anchors. Anchor position is indicated by purple arrows.



Extended Data Fig. 8 | See next page for caption.

Extended Data Fig. 8 | Supplementary E/P loop analyses. **a**, APA of the three clusters of E/P loops on merged and two biological replicates. Bin size, 10 kb. Numbers indicate average loop strength: $\ln(\text{obs}/\text{exp})$. **b**, Hi-C contact maps showing an additional example of cluster 1 E/P loop (chr1: 43.45 Mb–43.65 Mb, green arrow). Bin size, 10 kb. Colour bar denotes q -normed reads. Contact maps are coupled with genome browser tracks of CTCF and cohesin across all time points as well as asynchronous H3K4me3, H3K4me1 and H3K27ac and annotations of *cis*-regulatory elements. **c**, Similar to **b**, showing two examples of manually identified transient E/P contacts (*Pde12* locus and *Morc3* locus, indicated by red arrow). Boundaries or structural loop anchors that potentially interfere with these E/P contacts are indicated by black and blue arrows, respectively. Contact maps are coupled with tracks of Capture-C interaction profiles. Probes (anchor symbol) are located at promoters of *Pde12* and *Morc3* genes. **d**, Hi-C contact maps showing the *Pde12* locus on two biological replicates. Bin size, 10 kb. **e**, Quantification of the Capture-C read density of the red regions in **c**. $n = 3$ biological replicates. Data are mean \pm s.e.m. P values were calculated from two-sided Student's t -test. **f**, Similar to **d**, Hi-C contact maps showing the cluster 3 E/P loop (red arrows) at *Commd3* locus in two biological replicates. Potential interfering loop is indicated by blue arrows. **g**, Insulation score profiles centred around the boundaries and interfering structural loop anchors that solely reside within cluster 1, 2 or 3 E/P loops. **h**, Sanger

sequencing profiles showing deletion of the CTCF core motif at the upstream anchor of the structural loop (blue arrows in **f**) that potentially interfere with the cluster 3 E/P loop at the *Commd3* locus (red arrows in **f**). **i**, ChIP-qPCR showing the abrogation of CTCF and Rad21 binding at the edited site in **f**. $n = 3$ biological replicates. Data are mean \pm s.e.m. P values were calculated by two-sided Student's t -test. **j**, Schematic showing potential behaviour of cluster 3 E/P loops before and after deletion of the interfering structural loop anchor. **k**, Capture-C interaction profiles between *Commd3* promoter and downstream *cis*-regulatory element (red bars) on wild-type and interfering anchor-deleted mutant cells over time. The location of the capture probe is indicated by the anchor symbol. The deleted CTCF site is indicated by green triangles. Formation of the transient loop is indicated by red arches. **l**, Quantification showing read density of the red regions in **k**. $n = 3$ and 2 biological replicates for wild-type and mutant cells, respectively. Data are mean \pm s.e.m. P values were calculated by two-sided Student's t -test. **m**, Box plots showing ChIP-seq signals of indicated histone modifications at anchors that solely participate in cluster 1, 2 or 3 (transient) E/P loops ($n = 2, 612, 1, 338$ and 413 respectively). For all box plots, centre lines denote medians; box limits denote 25th–75th percentile; whiskers denote 5th–95th percentile. P values were calculated using a two-sided Mann-Whitney U -test.



Extended Data Fig. 9 | Relationship between post-mitotic structural organization and gene reactivation. a, Meta-region analysis of Pol II occupancy of active genes across all stages of the cell cycle. TSS, transcription start site; TES, transcription end site. **b**, Bin plots showing the positive correlation between Pol II ChIP-seq signal strength and eigenvector 1 (asynchronous G1E-ER4 cells²⁷, 25-kb binned) genome-wide. **c**, Left, schematic showing genes that are within early or late domains. Right, average Pol II occupancy of genes that reside in prometaphase ($n = 2,274$ genes) ana/telophase ($n = 2,114$ genes), early G1 ($n = 1,159$ genes) and mid G1 ($n = 303$ genes) emerging domains. Data are mean \pm 99% confidence interval. **d**, Heat map showing gene-body Pol II occupancy across all stages of the cell cycle. Genes are ranked by their PC1 values ('spikiness'). **e**, Genome browser tracks showing

representative examples of early spiking (*Kpna2*) and gradually activating (*Nedd4*) genes. **f**, Quantification of gene-body Pol II occupancy in **e**. $n = 2$ biological replicates for 0 h, and $n = 3$ biological replicates for other time points. Data are mean \pm s.e.m. **g**, Schematic showing the stratification of genes on the basis of their involvement in E/P loops. **h**, Table showing the number of genes that are solely involved in clusters of E/P loops. **i**, Average gene-body Pol II occupancy of the genes in **h** over time. Sample sizes are shown in **h**. Data are mean \pm s.e.m. **j**, Box plots showing the spikiness (PC1) of genes in **h**. Sample sizes are shown in **h**. For all box plots, centre lines denote medians; box limits denote 25th–75th percentile; whiskers denote 5th–95th percentile. P values were calculated using a two-sided Mann–Whitney U -test.

Reporting Summary

Nature Research wishes to improve the reproducibility of the work that we publish. This form provides structure for consistency and transparency in reporting. For further information on Nature Research policies, see [Authors & Referees](#) and the [Editorial Policy Checklist](#).

Statistics

For all statistical analyses, confirm that the following items are present in the figure legend, table legend, main text, or Methods section.

n/a Confirmed

- The exact sample size (n) for each experimental group/condition, given as a discrete number and unit of measurement
- A statement on whether measurements were taken from distinct samples or whether the same sample was measured repeatedly
- The statistical test(s) used AND whether they are one- or two-sided
Only common tests should be described solely by name; describe more complex techniques in the Methods section.
- A description of all covariates tested
- A description of any assumptions or corrections, such as tests of normality and adjustment for multiple comparisons
- A full description of the statistical parameters including central tendency (e.g. means) or other basic estimates (e.g. regression coefficient) AND variation (e.g. standard deviation) or associated estimates of uncertainty (e.g. confidence intervals)
- For null hypothesis testing, the test statistic (e.g. F , t , r) with confidence intervals, effect sizes, degrees of freedom and P value noted
Give P values as exact values whenever suitable.
- For Bayesian analysis, information on the choice of priors and Markov chain Monte Carlo settings
- For hierarchical and complex designs, identification of the appropriate level for tests and full reporting of outcomes
- Estimates of effect sizes (e.g. Cohen's d , Pearson's r), indicating how they were calculated

Our web collection on [statistics for biologists](#) contains articles on many of the points above.

Software and code

Policy information about [availability of computer code](#)

Data collection

For flow data collection, we used FACSDiva 8 (BD Biosciences) and Summit (Beckman Coulter)
For image collection, we used MetaMorph
For high-throughput sequencing data collection, we used NextSeq Control Software v2.2.0.

Data analysis

For statistical analyses, we used R (R studio) or GraphPad Prism 7.
For imaging processing, we used Fiji (Image J 2.0.0).
For flow chart generation, we used FlowJo 10.4.0.
For high throughput sequencing data processing and subsequent data analyses we used:
pandas 0.22.0,
scipy 0.19.1,
numpy 1.13.3,
HiC-Pro_2.7.7,
juicer_tools_0.7.5.jar, 0.7.0 jar
FastQC 0.11.5,
trim galore 0.4.1-0,
Cutadapt 1.18,
FLASH 1.2.8,
CCAnalyzer3,
bowtie
bowtie 0.12.7,
SAMtools v0.1.19,
macs2 v2.1.0, 2.1.1,
kent UCSC Utilities,
bwttool 1.0,
HOMER 4.9.1,

BEDtools,2.27.1

deeptools 2.5.4

For loop and stripe identification and DI+sweep. See method section (code is available upon request to the corresponding authors)

3D netmod domain calling: https://bitbucket.org/creminslab/3dnetmod_method_v3.0_development

rGMAP 1.4

For manuscripts utilizing custom algorithms or software that are central to the research but not yet described in published literature, software must be made available to editors/reviewers. We strongly encourage code deposition in a community repository (e.g. GitHub). See the Nature Research [guidelines for submitting code & software](#) for further information.

Data

Policy information about [availability of data](#)

All manuscripts must include a [data availability statement](#). This statement should provide the following information, where applicable:

- Accession codes, unique identifiers, or web links for publicly available datasets
- A list of figures that have associated raw data
- A description of any restrictions on data availability

All figures include publicly available data. All ChIP-seq, Capture-C and Hi-C raw and processed data generated from this study are now deposited into the GEO database with accession number GSE129997 for public access. ChIP-seq files of histone modifications shown in figure 4 and Extended data figures 7 and 8 are available from the GEO database with accession numbers: H3K27ac (GSE61349), H3K4me1 (GSM946535), H3K4me3 (GSM946533), H3K36me3 (GSM946529) and H3K9me3 (GSM946542)

Field-specific reporting

Please select the one below that is the best fit for your research. If you are not sure, read the appropriate sections before making your selection.

- Life sciences Behavioural & social sciences Ecological, evolutionary & environmental sciences

For a reference copy of the document with all sections, see [nature.com/documents/nr-reporting-summary-flat.pdf](https://www.nature.com/documents/nr-reporting-summary-flat.pdf)

Life sciences study design

All studies must disclose on these points even when the disclosure is negative.

Sample size	Sample size was not pre-determined. We used sample sizes commonly accepted for high throughput genome wide experiments. We performed 2 biological replicates for Hi-C, 2-3 biological replicates for ChIP-seq and ChIP-qPCR, and 2-3 biological replicates for Capture-C. Hi-C and ChIP-seq data were pooled for down-stream analyses.
Data exclusions	Experiments were done in multiple replicates. Replicates with technical failure were removed.
Replication	2 biological replicates for Hi-C and at least 2-3 biological replicates for ChIP-seq and capture-C were generated.
Randomization	Experiments were not randomized. No animal or human subjects were involved in this study.
Blinding	Researchers were not blind to group allocation. Blinding was not relevant to our study as no human subjects were involved.

Reporting for specific materials, systems and methods

We require information from authors about some types of materials, experimental systems and methods used in many studies. Here, indicate whether each material, system or method listed is relevant to your study. If you are not sure if a list item applies to your research, read the appropriate section before selecting a response.

Materials & experimental systems

n/a	Involved in the study
<input type="checkbox"/>	<input checked="" type="checkbox"/> Antibodies
<input type="checkbox"/>	<input checked="" type="checkbox"/> Eukaryotic cell lines
<input checked="" type="checkbox"/>	<input type="checkbox"/> Palaeontology
<input checked="" type="checkbox"/>	<input type="checkbox"/> Animals and other organisms
<input checked="" type="checkbox"/>	<input type="checkbox"/> Human research participants
<input checked="" type="checkbox"/>	<input type="checkbox"/> Clinical data

Methods

n/a	Involved in the study
<input type="checkbox"/>	<input checked="" type="checkbox"/> ChIP-seq
<input type="checkbox"/>	<input checked="" type="checkbox"/> Flow cytometry
<input checked="" type="checkbox"/>	<input type="checkbox"/> MRI-based neuroimaging

Antibodies

Antibodies used

anti-pMPM2 Millipore, catlog#: 05-368, Clone: MPM-2, multiple lots of antibodies were used. Dilution: 0.2ul/10million cells

anti-lamin B1 Abcam, catlog#: ab16048, Polyclonal, lot# GR-3214420-1. Dilution: 0.5ul/1million cells

anti-CTCF Millipore, catlog#: 07-729, Polyclonal, lot# 2887267. Dilution: 5-10ug/ChIP

anti-Rad21 Abcam, catlog#: ab992, Polyclonal, lot# GR214359-7. Dilution: 5-10ug/ChIP

anti-Pol II Cell Signaling, catlog#: 14958, Clone: D8L4Y, lot# 1. Dilution: 8ug/IP

F(ab')₂-goat anti-mouse secondary antibody, APC, Thermo Fisher Scientific, catelog#: 17-4010-82. Polyclonal, lot# 1997054. Dilution: 20ul/10million cells.

Fluorescein (FITC) AffiniPure Goat Anti-Rabbit IgG (H+L), Jackson ImmunoResearch, Code: 111-095-144, Polyclonal. Dilution: 0.5ul/1million cells

Validation

anti-pMPM2 Millipore, catlog#: 05-368, multiple lots of antibodies were used. This antibody has been claimed to react with mouse pMPM2 by the manufacturer.

anti-lamin B1 Abcam, catlog#: ab16048, lot# GR-3214420-1. This antibody has been claimed to react with mouse by the manufacturer. This antibody has been extensively used to assess lamin B1 distribution in the literature (eg. Klymenko et al. Leukemia. 2018). Our experiments also confirmed the correct nuclear peripheral distribution of lamin B1 in interphase cells using this antibody.

anti-CTCF Millipore, catlog#: 07-729, lot# 2887267. This antibody has been claimed to react with mouse and validated for ChIP-seq by the manufacturer. This antibody was also extensively used for ChIP-seq studies and confirmed to lose signal upon CTCF depletion in our hands and also by others (eg. Nora. et al. 2017)

anti-Rad21 Abcam, catlog#: ab992, lot# GR214359-7. This antibody has been claimed to react with mouse and validated for ChIP experiments by the manufacturer. This antibody was also confirmed to lose signal upon loss of Rad21 (Rao. et al. 2017).

anti-Pol II Cell Signaling, 14958, lot# 1. This antibody has been claimed to react with mouse and to be suitable for ChIP by the manufacture. This antibody has also been previously used in our lab (Behera et al. 2019, Cell Reports) and also by others for ChIP experiments (eg. Sun Y. et al. 2019, Science Advances.)

F(ab')₂-goat anti-mouse secondary antibody, APC, Thermo Fisher Scientific, catelog#: 17-4010-82. lot# 1997054. The manufacturer has tested this antibody to be suitable for immunofluorescence studies.

Fluorescein (FITC) AffiniPure Goat Anti-Rabbit IgG (H+L), Jackson ImmunoResearch, Code: 111-095-144. the manufacturer states that this antibody reacts with whole molecule rabbit IgG. This antibody has been previously used by other studies on mouse samples (eg. Li et al. eLife. 2018). We also confirmed that it's positive for immunofluorescence.

Eukaryotic cell lines

Policy information about [cell lines](#)

Cell line source(s)	The G1E-ER4 cell line was a gift from Mitchell Weiss' laboratory.
Authentication	We regularly confirm that these cells can be induced to undergo terminal erythroid differentiation.
Mycoplasma contamination	G1E-ER4 cells has been tested to be negative of Mycoplasma
Commonly misidentified lines (See ICLAC register)	The cell line used (G1E-ER4) is not in the ICLAC database

ChIP-seq

Data deposition

- Confirm that both raw and final processed data have been deposited in a public database such as [GEO](#).
- Confirm that you have deposited or provided access to graph files (e.g. BED files) for the called peaks.

Data access links
May remain private before publication.

The Hi-C, Capture-C and ChIP-seq data generated and analyzed in this study are deposited in GEO repository under accession number GSE129997 for public access.

Files in database submission

1899_1900-1_S1_Read1.fq.gz
 1899_1900-1_S1_Read2.fq.gz
 1899_1900-2_S1_Read1.fq.gz
 1899_1900-2_S1_Read2.fq.gz
 1899_1900-3_S1_Read1.fq.gz
 1899_1900-3_S1_Read2.fq.gz
 1899_1900-4_S1_Read1.fq.gz
 1899_1900-4_S1_Read2.fq.gz
 1901-1902-5_S1_Read1.fq.gz
 1901-1902-5_S1_Read2.fq.gz
 1901-1902-6_S1_Read1.fq.gz

1901-1902-6_S1_Read2.fq.gz
1901-1902-7_S1_Read1.fq.gz
1901-1902-7_S1_Read2.fq.gz
1901-1902-8_S1_Read1.fq.gz
1901-1902-8_S1_Read2.fq.gz
1903-1904-10_S1_Read1.fq.gz
1903-1904-10_S1_Read2.fq.gz
1903-1904-11_S1_Read1.fq.gz
1903-1904-11_S1_Read2.fq.gz
1903-1904-12_S1_Read1.fq.gz
1903-1904-12_S1_Read2.fq.gz
1903-1904-9_S1_Read1.fq.gz
1903-1904-9_S1_Read2.fq.gz
1900_1_S2_Read1.fq.gz
1900_1_S2_Read2.fq.gz
1900_2_S2_Read1.fq.gz
1900_2_S2_Read2.fq.gz
1900_3_S2_Read1.fq.gz
1900_3_S2_Read2.fq.gz
1900_4_S2_Read1.fq.gz
1900_4_S2_Read2.fq.gz
1902_5_S2_Read1.fq.gz
1902_5_S2_Read2.fq.gz
1902_6_S2_Read1.fq.gz
1902_6_S2_Read2.fq.gz
1902_7_S2_Read1.fq.gz
1902_7_S2_Read2.fq.gz
1902_8_S2_Read1.fq.gz
1902_8_S2_Read2.fq.gz
1904_9_S2_Read1.fq.gz
1904_9_S2_Read2.fq.gz
1904_10_S2_Read1.fq.gz
1904_10_S2_Read2.fq.gz
1904_11_S2_Read1.fq.gz
1904_11_S2_Read2.fq.gz
1904_12_S2_Read1.fq.gz
1904_12_S2_Read2.fq.gz
1530_run151_Read1.fastq.gz
1530_run151_Read2.fastq.gz
1573_run163_Read1.fastq.gz
1573_run163_Read2.fastq.gz
1573_run165_Read1.fastq.gz
1573_run165_Read2.fastq.gz
1554_run154_Read1.fastq.gz
1554_run154_Read2.fastq.gz
1554_run160_Read1.fastq.gz
1554_run160_Read2.fastq.gz
1554_run161_Read1.fastq.gz
1554_run161_Read2.fastq.gz
1554_run162_Read1.fastq.gz
1554_run162_Read2.fastq.gz
1531_run151_Read1.fastq.gz
1531_run151_Read2.fastq.gz
1574_run163_Read1.fastq.gz
1574_run163_Read2.fastq.gz
1574_run165_Read1.fastq.gz
1574_run165_Read2.fastq.gz
1555_run154_Read1.fastq.gz
1555_run154_Read2.fastq.gz
1555_run160_Read1.fastq.gz
1555_run160_Read2.fastq.gz
1555_run161_Read1.fastq.gz
1555_run161_Read2.fastq.gz
1555_run162_Read1.fastq.gz
1555_run162_Read2.fastq.gz
1536_run152_Read1.fastq.gz
1536_run152_Read2.fastq.gz
1536_run155_Read1.fastq.gz
1536_run155_Read2.fastq.gz
1536_run156_Read1.fastq.gz
1536_run156_Read2.fastq.gz
1556_run154_Read1.fastq.gz
1556_run154_Read2.fastq.gz
1556_run160_Read1.fastq.gz
1556_run160_Read2.fastq.gz

1556_run161_Read1.fastq.gz
1556_run161_Read2.fastq.gz
1556_run162_Read1.fastq.gz
1556_run162_Read2.fastq.gz
1537_run152_Read1.fastq.gz
1537_run152_Read2.fastq.gz
1537_run155_Read1.fastq.gz
1537_run155_Read2.fastq.gz
1537_run156_Read1.fastq.gz
1537_run156_Read2.fastq.gz
1557_run154_Read1.fastq.gz
1557_run154_Read2.fastq.gz
1557_run160_Read1.fastq.gz
1557_run160_Read2.fastq.gz
1557_run161_Read1.fastq.gz
1557_run161_Read2.fastq.gz
1557_run162_Read1.fastq.gz
1557_run162_Read2.fastq.gz
1533_run151_Read1.fastq.gz
1533_run151_Read2.fastq.gz
1533_run155_Read1.fastq.gz
1533_run155_Read2.fastq.gz
1533_run156_Read1.fastq.gz
1533_run156_Read2.fastq.gz
1558_run154_Read1.fastq.gz
1558_run154_Read2.fastq.gz
1558_run160_Read1.fastq.gz
1558_run160_Read2.fastq.gz
1558_run161_Read1.fastq.gz
1558_run161_Read2.fastq.gz
1558_run162_Read1.fastq.gz
1558_run162_Read2.fastq.gz
1930_S1_Read1.fq.gz
1930_S1_Read2.fq.gz
1931_S1_Read1.fq.gz
1931_S1_Read2.fq.gz
1932_S1_Read1.fq.gz
1932_S1_Read2.fq.gz
1933_S1_Read1.fq.gz
1933_S1_Read2.fq.gz
1934_S1_Read1.fq.gz
1934_S1_Read2.fq.gz
1935_S1_Read1.fq.gz
1935_S1_Read2.fq.gz
1936_S1_Read1.fq.gz
1936_S1_Read2.fq.gz
1937_S1_Read1.fq.gz
1937_S1_Read2.fq.gz
1930_S2_Read1.fq.gz
1930_S2_Read2.fq.gz
1931_S2_Read1.fq.gz
1931_S2_Read2.fq.gz
1932_S2_Read1.fq.gz
1932_S2_Read2.fq.gz
1933_S2_Read1.fq.gz
1933_S2_Read2.fq.gz
1934_S2_Read1.fq.gz
1934_S2_Read2.fq.gz
1935_S2_Read1.fq.gz
1935_S2_Read2.fq.gz
1936_S2_Read1.fq.gz
1936_S2_Read2.fq.gz
1937_S2_Read1.fq.gz
1937_S2_Read2.fq.gz
CTCF_asyn_Rep0.fastq
CTCF_asyn_Rep1.fastq
CTCF_prometa_Rep0.fastq
CTCF_prometa_Rep1.fastq
CTCF_prometa_Rep2.fastq
CTCF_anatelo_Rep5.fastq
CTCF_anatelo_Rep6.fastq
CTCF_earlyG1_Rep1.fastq
CTCF_earlyG1_Rep2.fastq
CTCF_midG1_Rep1.fastq
CTCF_midG1_Rep2.fastq

CTCF_lateG1_Rep1.fastq
CTCF_lateG1_Rep2.fastq
Rad21_asyn_Rep1.fastq
Rad21_asyn_rep3.fastq
Rad21_prometa_Rep3.fastq
Rad21_prometa_Rep4.fastq
Rad21_anatelo_Rep5.fastq
Rad21_anatelo_Rep6.fastq
Rad21_earlyG1_Rep1.fastq
Rad21_earlyG1_Rep5.fastq
Rad21_midG1_Rep1.fastq
Rad21_midG1_Rep3.fastq
Rad21_lateG1_Rep1.fastq
Rad21_lateG1_Rep3.fastq
wt_prometa_rep1_Read1.fq.gz
wt_prometa_rep2_Read1.fq.gz
wt_ana.telo_rep1_Read1.fq.gz
wt_ana.telo_rep2_Read1.fq.gz
wt_ana.telo_rep3_Read1.fq.gz
wt_early_g1_rep1_Read1.fq.gz
wt_early_g1_rep2_Read1.fq.gz
wt_early_g1_rep3_Read1.fq.gz
wt_mid_g1_rep1_Read1.fq.gz
wt_mid_g1_rep2_Read1.fq.gz
wt_mid_g1_rep3_Read1.fq.gz
wt_late_g1_rep1_Read1.fq.gz
wt_late_g1_rep2_Read1.fq.gz
wt_late_g1_rep3_Read1.fq.gz
input_asyn.fastq
input_prometa.fastq
input_anatelo.fastq
input_earlyG1.fastq
input_midG1.fastq
input_lateG1.fastq
capture_c_commd3_locus_wt_pro_meta_merged.bdg
capture_c_commd3_locus_wt_ana.telo_merged.bdg
capture_c_commd3_locus_wt_early_G1_merged.bdg
capture_c_commd3_locus_wt_mid_G1_merged.bdg
capture_c_morc3_locus_wt_pro_meta_merged.bdg
capture_c_morc3_locus_wt_ana.telo_merged.bdg
capture_c_morc3_locus_wt_early_G1_merged.bdg
capture_c_morc3_locus_wt_mid_G1_merged.bdg
capture_c_pde12_locus_wt_pro_meta_merged.bdg
capture_c_pde12_locus_wt_ana.telo_merged.bdg
capture_c_pde12_locus_wt_early_G1_merged.bdg
capture_c_pde12_locus_wt_mid_G1_merged.bdg
capture_c_slow_structural_loop_wt_pro_meta_merged.bedgraph
capture_c_slow_structural_loop_wt_ana.telo_merged.bedgraph
capture_c_slow_structural_loop_wt_early_G1_merged.bedgraph
capture_c_slow_structural_loop_wt_mid_G1_merged.bedgraph
capture_c_fast_structural_loop_wt_pro_meta_merged.bedgraph
capture_c_fast_structural_loop_wt_ana.telo_merged.bedgraph
capture_c_fast_structural_loop_wt_early_G1_merged.bedgraph
capture_c_fast_structural_loop_wt_mid_G1_merged.bedgraph
prometa_raw_intrachromosomal_contact_matrices.tar.gz
prometa_kr_intrachromosomal_contact_matrices.tar.gz
prometa_qnorm_intrachromosomal_contact_matrices.tar.gz
anatelo_raw_intrachromosomal_contact_matrices.tar.gz
anatelo_kr_intrachromosomal_contact_matrices.tar.gz
anatelo_qnorm_intrachromosomal_contact_matrices.tar.gz
earlyG1_raw_intrachromosomal_contact_matrices.tar.gz
earlyG1_kr_intrachromosomal_contact_matrices.tar.gz
earlyG1_qnorm_intrachromosomal_contact_matrices.tar.gz
midG1_raw_intrachromosomal_contact_matrices.tar.gz
midG1_kr_intrachromosomal_contact_matrices.tar.gz
midG1_qnorm_intrachromosomal_contact_matrices.tar.gz
lateG1_raw_intrachromosomal_contact_matrices.tar.gz
lateG1_kr_intrachromosomal_contact_matrices.tar.gz
lateG1_qnorm_intrachromosomal_contact_matrices.tar.gz
prometa_domains.bed
anatelo_domains.bed
earlyG1_domains.bed
midG1_domains.bed
lateG1_domains.bed
prometa_loops.tsv

```

anatelo_loops.tsv
earlyG1_loops.tsv
midG1_loops.tsv
lateG1_loops.tsv
prometa_stripes.tsv
anatelo_stripes.tsv
earlyG1_stripes.tsv
midG1_stripes.tsv
lateG1_stripes.tsv
CTCF_asyn.bw
CTCF_prometa.bw
CTCF_anatelo.bw
CTCF_earlyG1.bw
CTCF_midG1.bw
CTCF_lateG1.bw
Rad21_asyn.bw
Rad21_prometa.bw
Rad21_anatelo.bw
Rad21_earlyG1.bw
Rad21_midG1.bw
Rad21_lateG1.bw
CTCF_asyn.narrowPeak
CTCF_prometa.narrowPeak
CTCF_anatelo.narrowPeak
CTCF_earlyG1.narrowPeak
CTCF_midG1.narrowPeak
CTCF_lateG1.narrowPeak
Rad21_asyn.narrowPeak
Rad21_prometa.narrowPeak
Rad21_anatelo.narrowPeak
Rad21_earlyG1.narrowPeak
Rad21_midG1.narrowPeak
Rad21_lateG1.narrowPeak
capture_c_commd3_locus_commd3_mutant_prometa_merged.bdg
capture_c_commd3_locus_commd3_mutant_anateo_merged.bdg
capture_c_commd3_locus_commd3_mutant_early_g1_merged.bdg
capture_c_commd3_locus_commd3_mutant_mid_g1_merged.bdg
WT_Pol2_Noc0h.bw
WT_Pol2_Noc25min.bw
WT_Pol2_Noc1h.bw
WT_Pol2_Noc2h.bw
WT_Pol2_Noc4h.bw

```

Genome browser session
(e.g. [UCSC](https://genome.ucsc.edu))

<https://genome.ucsc.edu/s/thomasgilgenast/mitosis-ctcf-rad21-pol2-chipseq>

Methodology

Replicates

See methods section. Briefly, 2-3 biological replicates were generated per time point per antibody. Specifically:

For CTCF, we generated 2 biological replicates per time point except prometaphase, for which we performed 3 biological replicates.

For Rad21, we performed 2 biological replicates per time point.

For Pol II, we performed 3 biological replicates per time point except prometaphase, for which we performed 2 biological replicates.

Sequencing depth

See supplementary table 7

Antibodies

anti-CTCF Millipore, 07-729
anti-Rad21 Abcam, ab992
anti-Pol II Cell Signaling, 14958

Peak calling parameters

Sequencing reads were mapped to the reference mouse genome mm9 using bowtie (0.12.7, "-m 2 --tryhard"). Reads were filtered to remove non-uniquely mapped reads and PCR duplicates using Samtools (v0.1.19) and converted to bed format using BEDtools (v2.27.1, "bedtools bamtobed").

For CTCF and Rad21, filtered reads from each biological replicate were pooled together and down-sampled to equivalent read counts across all cell cycle stages. Peaks were identified using the MACS2 with punctate calling for both CTCF and Rad21 (p-values 1e-8 and 1e-4 respectively), using each IP's cell cycle stage matched input as the control.

For Pol II, Peaks were then called with MACS2 for each replicate with a p-value cutoff of 1e-4, using each IP's cell cycle stage matched input as the control.

Data quality	<ol style="list-style-type: none"> (1). Raw fastq files were assessed with FastQC (v0.11.5) prior to processing. (2). Peaks were called using input controls corresponding to every cell cycle stage. (3). Peaks were called using p-value cutoffs described above and the default above 5-fold enrichment. (4). Correlation among replicates was assessed (Extended Data Fig. 1g-i). (5). Peaks of Rad21 and CTCF were largely overlapping and motif analysis revealed the expected CTCF motif within peaks. (6). Peaks of Pol II were largely located at expected genomic regions (TSS, genebodies).
Software	For CHIP-seq data processing and analyses, we used bowtie version 0.12.7, Samtools v0.1.19, macs2 2.1.1, 2.1.0, kent UCSC Utilities, bwtool version 1.0, HOMER version 4.9.1, BEDtools and deeptools 2.5.4

Flow Cytometry

Plots

Confirm that:

- The axis labels state the marker and fluorochrome used (e.g. CD4-FITC).
- The axis scales are clearly visible. Include numbers along axes only for bottom left plot of group (a 'group' is an analysis of identical markers).
- All plots are contour plots with outliers or pseudocolor plots.
- A numerical value for number of cells or percentage (with statistics) is provided.

Methodology

Sample preparation	See method section. Briefly, actively proliferating G1E-ER4 cells were synchronized at pro-metaphase with nocodazole treatment. Cells were then released from nocodazole for several durations (0h, 25min, 1h, 2h and 4h). Cells were harvested, washed with PBS and crosslinked with 1% PFA for 10min. Crosslinks were quenched with glycine for 5min and cells were then penetrated with 0.1% Triton X-100. Finally, cells were stained with 20ng/ml DAPI and subjected to cell sorting.
Instrument	Beckman Coulter Moflo Astrios sorter/Becton Dickinson FACSAria Fusion sorter
Software	Flow charts were generated using FlowJo 10.4.0
Cell population abundance	We achieved very high cell purity of pro-metaphase populations. The purity of pro-metaphase cells was >98%. This was confirmed by DAPI staining and the disassembly of lamin B1.
Gating strategy	Prometaphase cells were gated on mcherry (high), DAPI (4N) and pMPM2 (high) fluorescent signal. ana/telophase cells were gated based on DAPI (4N) and mcherry (low, relative to prometaphase) signals. G1 samples were gated based on DAPI (2N) and mcherry (low) signals.

- Tick this box to confirm that a figure exemplifying the gating strategy is provided in the Supplementary Information.